Eur. Phys. J. B (2014) 87: 260
DOI: 10.1140/epjb/e2014-50515-4

THE EUROPEAN
PHYSICAL JOURNAL B

Colloquium

Advances in femto-nano-optics: ultrafast nonlinearity of metal nanoparticles

Tatjana Stoll, Paolo Maioli[a], Aurélien Crut, Natalia Del Fatti, and Fabrice Vallée

FemtoNanoOptics group, Institut Lumière Matière UMR5306, Université Lyon 1, CNRS, 69622 Villeurbanne, France

Received 30 July 2014 / Received in final form 9 September 2014

Abstract. With the recent advances of experimental techniques, the nonlinear ultrafast optical response of metal nano-objects can now be investigated both on ensembles and on single nanoparticles. Its connection with the metal electronic and lattice kinetics is studied on the basis of a model describing the wavelength and time-dependent modifications of the object material dielectric function. Its application is illustrated in the case of single silver nanospheres and gold nanorods, as well as on ensembles of noble metal nanoparticles and metal-semiconductor nano-hybrids. This quantitative analysis also permits to elucidate the physical mechanisms at the origin of ultrafast nonlinearities in confined metals at different timescales.

1 Introduction

Synthesis of small particles with dimensions decreasing down to few nanometers and the simultaneous appearance of original physical and chemical effects has led to the investigation of a wide variety of different nanosystems, playing with the shape, size, composition and internal structure of nano-objects and their interactions with their environment. Fundamental studies on different materials have allowed to determine both experimentally and theoretically by which mechanisms size reduction affects physical properties. In the case of metal nanoparticles, the most striking effect of spatial confinement is the appearance of the localized surface plasmon resonance (SPR), deeply affecting their color [1–5]. This resonance, associated to a collective electron motion, results in a strong enhancement and spatial localization of the electromagnetic fields inside and around metal nanoparticles.

Additionally, confinement to the nanometric scale impacts the internal dynamical processes of nanosystems. This is in particular the case for the dynamics of electrons after an initial excitation (internal electron gas thermalization and electron energy loss by interactions with phonons [6–12]). Other phenomena, such as the ionic lattice mechanical response (phonon acoustic vibrations) [13–16] or thermal energy transfer processes (heat dissipation to the environment) [17] are also modified by size reduction [18,19]. These physical processes lead to a modification of some sensitive physical parameters (e.g., electronic energy distribution, nano-object shape and volume...), having as a direct consequence a variation of the nano-object dielectric functions. This in turn directly affects the optical response of nanoparticles (e.g., their light absorption or scattering) thus yielding the possibility of monitoring and characterizing ultrafast processes by measuring its time evolution by time-resolved optical spectroscopy [7,20]. This experimental approach, which has been initially developed for the investigation of internal dynamics of bulk metals [6,21,22], has been largely extended in the last two decades to the study of metal nanosystems through ensemble [7,15,23–25] and single nanoparticle [26–34] experiments (Figs. 1a and 1b). Many physical processes have been addressed by this method, such as light excitation-electronic motion coupling and coherence loss [35], SPR polarization decay [36,37],

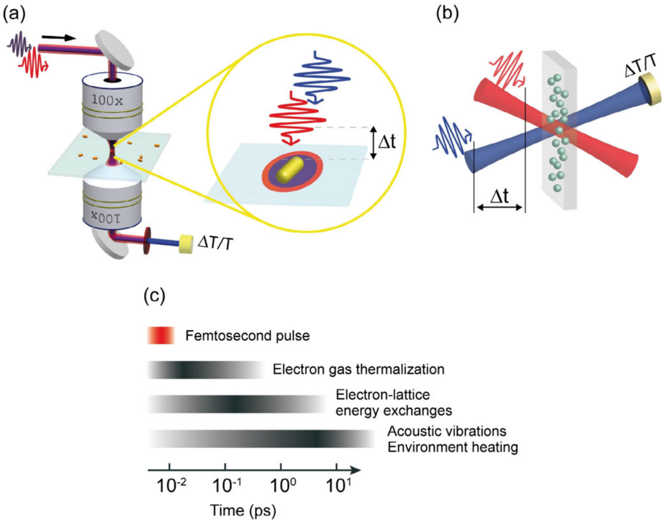

Fig. 1. Pump-probe optical spectroscopy setup for single (a) and ensemble (b) experiments. (c) Typical timescales of dynamical processes under investigation.

---

[a] e-mail: `paolo.maioli@univ-lyon1.fr`

electron-electron scattering and electron-lattice energy transfer [11,12,15,20,27,34,38], lattice acoustic vibrations and nanoparticle cooling [8,15,18,26,28,29,31,39–47], opening the possibility of elucidating fundamental mechanisms governing acoustic mode damping or heat transfer at the metal-matrix interface [48–52] (Fig. 1c). These investigations have also helped understanding the physical origins of the optical nonlinearities in metal nanoparticles and discriminating the effects of different electronic contributions (e.g. light-induced SPR broadening, frequency shift and increased electron-surface scattering) [53].

The accurate study of metal nanoparticle internal dynamics through the measurement of their time-resolved optical response requires detailed modeling of the physical processes involved, which is the main scope of this colloquium paper. In particular, a quantitative model must include the impact of the out-of-equilibrium conditions (electron excitation and subsequent lattice heating) on the electron energy distribution, the induced modifications of the metal dielectric function, and their influence on the nanoparticle optical response, taking plasmonic effects into account.

The optical response of a small-sized object is characterized by its absorption and scattering cross-sections, σ_{abs} and σ_{sca}, defined as the ratio between absorbed/scattered powers and the intensity of the light beam incident on the particle, extinction cross-section σ_{ext} being the sum of σ_{abs} and σ_{sca} [54]. Ultrafast excitation of the nanoparticle leads to a time-dependent modification of σ_{ext}, which is investigated by time-resolved spectroscopy. Experiments with femtosecond pump-probe setup carried out both on ensembles and on single metal nano-objects (Figs. 1a and 1b) followed analogous experimental approaches [7,15]. They consist in exciting the nanoparticles with a first laser pulse (pump) and monitoring the subsequent time-dependent modification of their absorption and/or scattering by measuring the transmission (or reflection) of a second time-delayed pulse (probe). By neglecting the influence of environment heating [18] and assuming weak induced changes in the nanoparticle, the $\Delta\sigma_{ext}$ variation, at probe wavelength λ and pump-probe time delay t, can thus be expressed as [20]:

$$\begin{aligned}\Delta\sigma_{ext}(\lambda,t) &= \frac{\partial\sigma_{ext}}{\partial\varepsilon_1}(\lambda)\,\Delta\varepsilon_1(\lambda,t)+\frac{\partial\sigma_{ext}}{\partial\varepsilon_2}(\lambda)\,\Delta\varepsilon_2(\lambda,t)\\ &= a_1(\lambda)\,\Delta\varepsilon_1(\lambda,t)+a_2(\lambda)\,\Delta\varepsilon_2(\lambda,t)\end{aligned} \tag{1}$$

$a_{1,2}$ being the stationary spectral-dependent plasmonic-enhanced σ_{ext} derivatives and $\Delta\varepsilon_{1,2}$ the dynamical spectral- and time-dependent pump-induced variations of the nanoparticle real and imaginary dielectric functions. Time-resolved signals result from a combination (Eq. (1)) of the dynamical physical effects under study, which induce variations $\Delta\varepsilon_{1,2}$ of dielectric functions, and their optical detection, with a spectral sensitivity given by $a_{1,2}$.

2 Dielectric function of metal nanoparticles

The dielectric functions $\varepsilon_{1,2}(\lambda)$ describe the interaction of the electrons with an incident electromagnetic field of wavelength λ. In the case of noble metals, they can be split in two contributions, corresponding to interaction of the field with electrons in the conduction band (Drude term) and to photoexcited transitions of bound electrons from inner electronic bands (interband contribution), the total dielectric function $\varepsilon(\lambda)$ being thus given by $\varepsilon(\lambda) = 1+[\chi^D(\lambda)+\chi^{ib}(\lambda)] = \varepsilon^D(\lambda)+\varepsilon^{ib}(\lambda)-1$, $\chi^{D,ib}(\lambda)$ being the Drude and interband susceptibilities of the medium.

Electrons in the conduction band can be approximated as a quasi-free electron gas, their contribution to the dielectric function being [55]:

$$\begin{aligned}\varepsilon^D(\lambda) &= 1-\frac{\lambda^2}{\lambda_p^2}\frac{1}{1+i\lambda\tau_n^{-1}/(2\pi c)}\\ \varepsilon_1^D(\lambda) &\approx 1-\frac{\lambda^2}{\lambda_p^2},\quad \varepsilon_2^D(\lambda)\approx\frac{\lambda^3}{2\pi c\lambda_p^2}\tau_n^{-1}\end{aligned} \tag{2}$$

where ε_1^D and ε_2^D are the real and imaginary parts of the metal dielectric functions, respectively, and λ_p is the plasma wavelength ($\lambda_p = 2\pi c\sqrt{m_e\varepsilon_0/n_e e^2}$, n_e being the density of conduction electrons, m_e and e the electron effective mass and electric charge, c the speed of light in vacuum and ε_0 the vacuum permittivity). As the momentum of a photon is negligibly small, photon absorption by a conduction electron requires the implication of a third particle, such as an auxiliary electron, a phonon of the ionic lattice or a defect in order to satisfy energy and momentum conservation. The imaginary part of the Drude term reflects these scattering processes, with different contributions dependent on the incoming photon wavelength λ and on the electronic and lattice temperatures (T_e and T_L), the characteristic optical scattering rate τ_n^{-1} for a nanoparticle being:

$$\begin{aligned}\tau_n^{-1}(\lambda,T_e,T_L) &= \tau_{e-ph}^{-1}(\lambda,T_e,T_L)+\tau_{e-e}^{-1}(\lambda,T_e)\\ &\quad+\tau_{e-S}^{-1}(\lambda,T_e)\end{aligned} \tag{3}$$

electron-defect scattering being neglected here. The dominant contribution to τ_n^{-1} comes from the electron-phonon scattering term τ_{e-ph}^{-1} [56–58]. It has been computed modeling electron-phonon interaction via a deformation potential, which connects the zero energy at the bottom of the conduction band to the lattice periodic deformation induced by phonon vibrations. As the energy of the phonons (a few meV) is small compared to optical photons (eV), they significantly modify only the momentum of excited electrons.

Accordingly, τ_{e-e}^{-1} describes the electron-electron scattering assisted photon-absorption rate. The auxiliary electron again enhances the light absorption by providing extra momentum. Only umklapp processes (electron-electron scattering by exchange of a vector in the reciprocal lattice) affect this term, whose contribution to τ_n^{-1} is however small [59].

The last term τ_{e-S}^{-1} is specific of confined systems and becomes relevant only for nanoparticles with sizes comparable or smaller than the conduction electron free path (~30 nm) [1,2]. This scattering term is a consequence of electron confinement [1,60] and thus depends on nanoparticle size and geometry. For a sphere or a symmetrical elongated nano-object (as a spheroid or a nanorod):

$$\tau_{e-S}^{-1}(\lambda, T_e) = 2g(\lambda, T_e)\, v_F / D_{eq} \tag{4}$$

where v_F is the conduction electron velocity at Fermi energy (1.4×10^6 m/s for Au and Ag) and $D_{eq} = \sqrt{S_{np}/\pi}$ is the nano-object equivalent diameter (where S_{np} is the nanoparticle surface) [61,62]. In a classical picture, τ_{e-S}^{-1} describes optical absorption assisted by electron-surface scattering. More quantum mechanically, it is associated to allowed optical transitions between confined states, the wave vector k being no longer a good quantum number [1,60,63]. The amplitude of this effect, for electrons confined in an infinite spherical potential (surface confinement) and not too small particles (so that conduction band states form a quasi-continuum), is given by [53,64]:

$$g(\lambda, T_e) = \frac{\lambda}{hcE_F^2} \int_0^{\infty} E^{3/2} \sqrt{E + hc/\lambda}\, f(E, T_e) \times [1 - f(E + hc/\lambda, T_e)]\, dE, \tag{5}$$

where E_F is the Fermi energy and $f(E, T_e)$ the temperature-dependent electron level occupation number. For noble metals, $g \sim 0.7$ at room temperature in the optical domain. This value is consistent with that measured in recent experiments, accounting for the explicit size dependence of τ_{e-S}^{-1} (Eq. (4)), but also for possible size-dependent modifications of τ_{e-ph}^{-1} and τ_{e-e}^{-1} (Eq. (3)) [61,65,66].

The term $\varepsilon^{ib}(\lambda)$ is associated to interband transitions of electrons from low energy bands (e.g. localized *d*-band) to higher energy ones, corresponding to quasi-free electron states. In the case of noble metals, *d*-states to conduction band transition thresholds lie at approximately 650 and 320 nm for gold and silver, respectively [67,68]. For wavelengths shorter than these values, absorption of one photon thus promotes an electron into the conduction band. The interband transition contribution to the stationary absorption spectrum can be computed through theoretical models starting from the band structure [69–72]. In the case of Au, interband absorption in the visible range mainly involves electrons localized around the L and X points of the Brillouin zone [67,73]. In the vicinity of the L point, visible light can be resonant with transitions both from occupied states in the *d*-bands to *p*-band quasi-free states ($L_{5+6+} \rightarrow L_{4-}$) and from *p*-band to *s*-band ($L_{4-} \rightarrow L_{4+}$), while a *d*-band to *p*-band transition ($X_{7+} \rightarrow X_{6-}$) dominates around the X point. In the case of Ag, only the two transitions around the L point can be excited by visible photons [68,74]. Band energy structure can be directly connected to the ε_2^{ib} absorption spectrum by integrating, for all k values in the Brillouin zone, the probability of a transition from occupied to unoccupied states with an energy separation corresponding to the incoming photon energy hc/λ. The probability of transitions from bands i to j is given by the joint density of states $J_{i\rightarrow j}$ ($\mathrm{J^{-1}\ m^{-3}}$) [72]:

$$J_{i\rightarrow j}(\lambda) = \int_{E_{\min}^{ij}}^{E_{\max}^{ij}} D_{i\rightarrow j}(E, \lambda)\, [f_i(E) - f_j(E + hc/\lambda)]\, dE \tag{6}$$

where $f_{i,j}$ are the occupation numbers of bands i and j and $D_{i\rightarrow j}$ is the energy dependent joint density of states for a transition with wavelength λ. Integration limits are specifically chosen so as to include all possible transitions from i to j band. By summing over all resonant interband transitions, the imaginary part of the Au dielectric constant is given by [69–72,75]:

$$\varepsilon_2^{ib}(\lambda) = \frac{e^2\lambda^2}{\varepsilon_0 m_e^2 c^2} \Big[A_{d\rightarrow p}^{X} J_{d\rightarrow p}^{X}(\lambda) + A_{d\rightarrow p}^{L} J_{d\rightarrow p}^{L}(\lambda) + A_{p\rightarrow s}^{L} J_{p\rightarrow s}^{L}(\lambda) \Big] \tag{7}$$

the one for Ag having a similar expression, with no X point contribution. $A_{i\rightarrow j}^{X,L}$ are the squares of the momentum operator matrix element describing the transition strengths. Their determination can be performed by combining an experimentally measured $\varepsilon_2(\lambda)$ dataset and the energy band structure (determined either theoretically or experimentally). The fit of $\varepsilon_2(\lambda)$ by the sum of interband (Eqs. (6) and (7)) and Drude (Eq. (2), dominant in the infrared range and negligible for visible light) contributions allows estimation of $A_{i\rightarrow j}^{X,L}$ values. This analysis is essential for quantitative computations of the transient time-resolved optical response $\Delta\varepsilon_1(\lambda, t)$ and $\Delta\varepsilon_2(\lambda, t)$ (see Sect. 5.1 below).

In the case of Au, the most common dielectric constant table is the one measured by Johnson and Christy [76]. It is still widely adopted for modeling optical properties of Au nanosystems as it predicts their spectral characteristics (SPR position and width) reasonably well, which is also the case for more recently measured sets [77–79]. For calculating the joint density of states, the Christensen and Seraphin [67] Au band structure has been most traditionally employed. In this work, the fit is based on the more recent relativistic band structure calculations by Rangel et al. [80], which give comparable results (Fig. 2a). The effective masses, describing the energy over k dependence, are computed from the band structure, while the energy gaps at the center of L and X Brillouin zone points are left as free parameters [73], as their precise experimental determination is difficult and the computed values sensitively depend on the model considered (e.g. choice of exchange-correlation potential in DFT theory) [80]. Note that, in the case of Au, the fit extends only in the visible region from 1 to 3.8 eV, where the only relevant contributions come from the transitions specified above. For a fit over a more extended energy range, additional interband transitions must be considered. In the case of Ag, experimental tables both by Johnson and Christy [76] and Palik [81] have been commonly used, the latter better reproducing experimentally measured SPR positions (mainly set by ε_1^{ib} values), the former being more

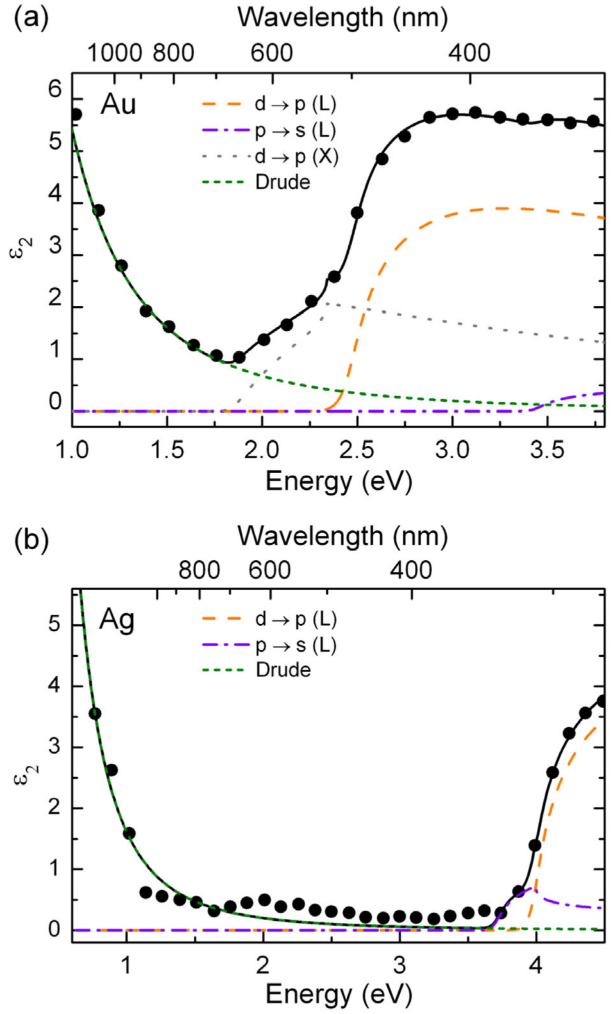

Fig. 2. Dots: experimental bulk ε_2 dielectric functions of Au (a) and Ag (b) [76]. Lines: fits taking into account interband contributions around the L and X points of the Brillouin zone and Drude term (see main text). Fit parameters are summarized in Table 1.

compatible for resonance widths (ε_2^{ib}) [82]. Recent experimental investigations failed to provide Ag dielectric constant sets better reproducing nanoparticle plasmon resonances, probably because of the sensitivity of dielectric constants to the quality and crystallinity of silver samples. Fits of Johnson and Christy constants with the effective masses derived from the energy band structure by Christensen for Ag [68] over the range from 0.6 to 4.5 eV will be used in the following (Fig. 2b). Values of effective masses used for the fits and the deduced optical gaps and $A_{i\to j}^{X,L}$ matrix elements are summarized in Table 1.

3 Optical absorption of metal nanoparticles

To determine $a_{1,2}$ values (Eq. (1)), the σ_{ext} extinction cross-section of a matrix-embedded nano-object and its dependence on $\varepsilon_{1,2}$ must be computed. For dimensions much smaller than incident light wavelength, the electromagnetic response of a nanoparticle can be approximated as the one of a dipole $\boldsymbol{p}(\lambda)$ at the center of the object aligned with the external oscillating electric field $\boldsymbol{E}(\lambda)$ (dipolar approximation). In this case:

$$\boldsymbol{p}(\lambda) = \varepsilon_0\,\varepsilon_m\,\tilde{\alpha}(\lambda)\;\boldsymbol{E}(\lambda) \qquad (8)$$

where $\tilde{\alpha}$ is the linear polarizability of the nano-object and ε_m the dimensionless matrix dielectric constant. In the general case of a small elongated nanoparticle, as an ellipsoid or a spheroid (i.e. ellipsoid with two axes of equal length), the linear polarizability takes the form [1,5,54]:

$$\tilde{\alpha}(\lambda) = \frac{V_{np}}{L_i}\frac{\varepsilon(\lambda)-\varepsilon_m}{\varepsilon(\lambda)+[(1-L_i)/L_i]\,\varepsilon_m} \qquad (9)$$

where $V_{np} = (4\pi/3)abc$ is the nanoparticle volume (a, b and c being the semi-axes of the ellipsoid), and L_i is a factor depending on particle geometry and incident light polarization. In the case of a nanosphere, $L_i = 1/3$ independently of orientation. For a prolate spheroid (i.e. elongated cigar-like nanoparticle with $a > b = c$) and light polarization parallel to its long axis (x direction), L_i writes:

$$L_x = \frac{1-e^2}{e^2}\left[-1+\frac{1}{2e}\ln\left(\frac{1+e}{1-e}\right)\right] \qquad (10)$$

with eccentricity $e^2 = 1-(b/a)^2$ and $L_y = L_z = (1-L_x)/2$. Within the small size approximation, the extinction cross-section of a nano-object can be identified with its absorption cross-section, the scattering one becoming negligible (as it scales with V_{np}^2, while absorption is proportional to V_{np}) [54]. Absorption being proportional to the imaginary part of the polarizability, one obtains:

$$\begin{aligned}\sigma_{ext}(\lambda) \approx \sigma_{abs}(\lambda) &= \frac{2\pi}{\lambda}\sqrt{\varepsilon_m}\,\mathrm{Im}\left[\tilde{\alpha}(\lambda)\right]\\ &= \frac{2\pi V\varepsilon_m^{3/2}}{\lambda L_i^2}\frac{\varepsilon_2(\lambda)}{\left[\varepsilon_1(\lambda)+(1-L_i)/L_i\varepsilon_m\right]^2+\varepsilon_2^2(\lambda)}.\end{aligned} \qquad (11)$$

For weak or weakly dispersed ε_2, vanishing of the first term in the denominator corresponds to a resonant enhancement of the absorption. By combining equations (2) and (11), the surface plasmon resonance condition can be expressed as [39,83]:

$$\lambda_{SPR} = \lambda_p\sqrt{\varepsilon_1^{ib}(\lambda_{SPR})+\frac{1-L_i}{L_i}\varepsilon_m}. \qquad (12)$$

For gold nanospheres, the SPR lies in the green part of the spectrum, at wavelengths ranging from 500 to 540 nm depending on the environment (through the dielectric constant ε_m, Eq. (12)). It thus overlaps the domain of interband transitions (Fig. 2a), whose threshold is around $\lambda_{ib} \approx 650$ nm. This is illustrated by Figure 3a, showing the extinction cross-section of a 30 nm Au nanosphere in water ($\varepsilon_m = 1.77$) computed in the dipolar approximation (dotted line in Fig. 3a). To take into account

Table 1. Effective masses (in unity of electron mass m$_0$), band energies and relative oscillator strengths $\eta^{X,L}_{i\to j} = A^{X,L}_{i\to j}/A^{L}_{d\to p}$ at points L and X of the Brillouin zone for Au and Ag (band symmetry labels from Refs. [68,73]). Effective masses were computed from Au [80] and Ag [68] band structures. Energy positions with respect to the Fermi energy were deduced from the fit of the corresponding dielectric constants [76] (see Fig. 2). Drude quasi-free electron parameters are also reported for the two metals.

Band		‖ Mass (m$_0$)	⊥ Mass (m$_0$)	Energy (eV)	$\eta^{X,L}_{i\to j}$
Au L Point					
4^+	(s)	+0.101	–6.797	+3.414	$\eta^{L}_{p\to s} = 0.272$
4^-	(p)	–0.157	+0.146	–1.368	$\eta^{L}_{d\to p} = 1$
$5^+ + 6^+$	(d)	–1.326	–0.499	–2.055	
Au X Point					
6^-	(p)	–0.125	+0.166	+0.573	$\eta^{X}_{d\to p} = 0.320$
7^+	(d)	–0.944	–0.446	–1.767	
Ag L Point					
4^+	(s)	+0.128	+5.160	+3.684	$\eta^{L}_{p\to s} = 0.478$
4^-	(p)	–0.172	+0.320	–0.310	$\eta^{L}_{d\to p} = 1$
$5^+ + 6^+$	(d)	–2.075	–2.580	–3.942	
Drude contribution					
Au		$\lambda_p = 138$ nm, $\hbar\tau_n^{-1} = 20$ meV, $E_F = 5.49$ eV			
Ag		$\lambda_p = 138$ nm, $\hbar\tau_n^{-1} = 67$ meV, $E_F = 5.53$ eV			

confinement effects on the dielectric constants, the bulk $\varepsilon_2^D(\lambda)$ contribution (Eqs. (2) to (4) with $D_{eq} \to \infty$) was subtracted to the experimental bulk Au dielectric constant values and replaced by its D_{eq} dependent expression [84], using $g = 0.7$. Exact calculations of $\sigma_{ext}(\lambda)$ using Mie theory [54] give a more precise prediction of the extinction spectrum (Fig. 3a, solid line). A slight difference appears between the two spectra, the discrepancy being expected to increase for larger dimensions. a_1 and a_2 derivative profiles (Fig. 3a, dashed and dash-dotted line, respectively), computed by numerical derivation of the Mie theory spectrum (very similar profiles are obtained within dipolar approximation by derivating Eq. (11) with respect to $\varepsilon_{1,2}$), are visibly enhanced around λ_{SPR}, thus increasing the amplitude of time-resolved transient optical signals $\Delta\sigma_{ext}$ around λ_{SPR} (Eq. (1)). In the case of a 30 nm Ag nanosphere (Fig. 3b) a larger shift ($\Delta\lambda_{SPR} \approx$ 2 and 10 nm for 30 nm Au and Ag nanospheres, respectively) and broadening appear when comparing dipolar approximation (dotted line) and Mie theory modeling (solid line). This results from the higher polarizability of the Ag sphere at λ_{SPR} (Eq. (9)), enhancing both radiative damping and retardation effects (responsible for the resonance broadening and red-shift, respectively [2]). The plasmon resonance of an elongated symmetrical object, as a nanorod or a prolate spheroid with incoming light polarized parallel to the main axis (Fig. 3c), sensitively shifts with increasing aspect ratio $\eta = a/b$ [3,85,86]. This provides a convenient way of tuning the Au resonance out of interband transitions, thus narrowing the resonance linewidth [62,87–89]. As for spherical nano-objects, the spectrum computed in dipolar approximation (Fig. 3c, dotted line, with $2a = 43$ nm and $\eta = 3.58$) can be compared to the one given by an exact theory (extension of Mie theory for spheroids), which has been developed by solving Maxwell's equations in spheroidal coordinates (Fig. 3c, solid line) [90]. For nano-objects with arbitrary shapes, optical properties can be computed numerically using different approaches, one of the most common being Finite Element Method (Fig. 3d) [91]. When applied to computing the optical response of a gold nanorod, numerical calculations show the same behavior as for prolate spheroids, i.e., for light parallel to its long axis, SPR shift to higher wavelengths with increasing aspect ratio (Fig. 3d), its derivatives a_1 and a_2 also being centered at the nanorod SPR.

In conclusion, for all considered shapes and metals, the localized surface plasmon resonance induced by electron dielectric confinement leads to a strong enhancement of both the linear extinction spectrum and its derivatives ruling the amplitude of the out-of-equilibrium nonlinear response (Eq. (1)). The dispersion-like a_1 profile (red dashed lines) always crosses the horizontal axis near λ_{SPR}. Its spectral dependence has the same profile as the $\sigma_{ext}(\lambda)$ direct derivative with respect to λ, as deduced from equations (2) and (11) by neglecting spectral dispersion of the ε_1^{ib} contribution, which yields $a_1(\lambda) \approx \partial\sigma_{ext}/\partial\lambda|_\lambda \left(-\lambda_p^2/2\lambda\right)$. The a_1 spectral derivative is thus proportional to both the amplitude of the SPR and its quality factor [32].

4 Ultrafast electron kinetics

Differential $\Delta\varepsilon_{1,2}(\lambda, t)$ terms in equation (1) reflect the dynamics of the system, i.e. its temporal response after an initial ultrafast excitation by the pump pulse. After discussion of energy injection into the system and relaxation via electronic interactions, we will consider in Section 5 how this kinetics affects the dielectric function of the metal nanoparticles, i.e. induces the transient $\Delta\varepsilon_{1,2}(\lambda, t)$ optical response.

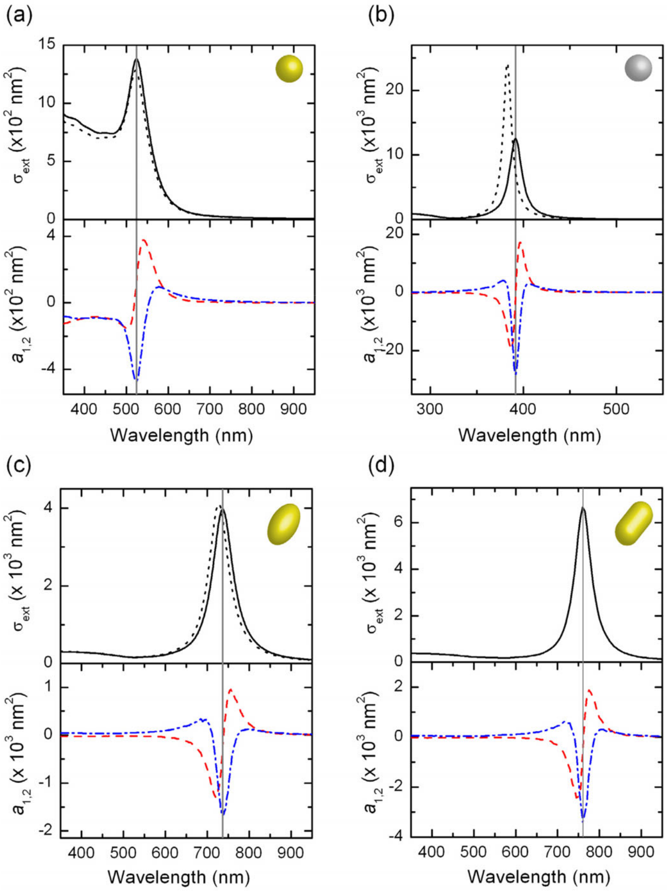

Fig. 3. Computed extinction cross-sections and their a_1 and a_2 derivatives for a 30 nm diameter Au sphere (a), 30 nm diameter Ag sphere (b), 43×12 nm Au prolate spheroid (c) and 43×12 nm Au nanorod (d). The vertical lines indicate λ_{SPR}. Upper panels: full lines correspond to exact calculations based on Mie theory ((a) and (b)), on its extension in spheroidal coordinates (c) and on FEM computing (d). For comparison, black dotted lines are calculations based on dipolar approximation. Lower panels: red dashed (blue dash-dotted) lines represent a_1 (a_2) terms, obtained by ε_1 (ε_2) derivation of extinction cross-sections. The electron-surface scattering parameter g is chosen equal to 0.7 (Eq. (4)).

The most adapted physical quantity to describe the electronic dynamics in a metal nanosystem is the time- and energy-dependent distribution function $f(E,t)$ of electron energy states. As in bulk materials, its variation with time is described by the Boltzmann equation. Assuming an isotropic parabolic conduction band it writes [6,22,92]:

$$\frac{df\,(E,t)}{dt} = \left.\frac{\partial f\,(E,t)}{\partial t}\right|_{exc} + \left.\frac{\partial f\,(E,t)}{\partial t}\right|_{e-e} + \left.\frac{\partial f\,(E,t)}{\partial t}\right|_{e-ph} \tag{13}$$

where the different terms account for electron occupation number evolution by initial pulse excitation, internal thermalization by electron-electron scattering and electron energy transfer to the lattice through electron-phonon coupling, respectively. The electron energy in metal nanoparticles can also be directly dumped to the surrounding matrix (solvent or glass). However, this process will not be considered here as it is slower and only relevant for small nanoparticles and strong excitations [93,94].

Equation (13) is solved with an initial condition corresponding to thermalized conduction electrons (at a temperature T_0 of typically 300 K), $f(E, t = -\infty)$ being thus described by a Fermi-Dirac distribution, with states occupied from the bottom of the energy band to approximately Fermi energy ($E_F \approx 5.5$ eV for Au and Ag). Neglecting coherent electron-light coupling that takes place on a very short timescale [6,35,95], the excitation can be described in terms of quasi-free electron absorption. For pump pulse energies lower than the interband transition threshold ($\lambda_{pump} > \lambda_{ib}$), electron-hole pairs are generated only in the conduction band. Electrons are thus described by an athermal distribution, with a small fraction of electrons having absorbed a photon promoted to an energy exceeding E_F, most of the electrons still occupying initial unperturbed states. The first term in the Boltzmann equation (Eq. (13)) describes this excitation process accounting for the specific temporal dependence of the excitation pulse (typical durations of 20 to 100 fs, see Fig. 1c) [6,22]. Even though at this stage an electronic temperature cannot be defined, the excited electron distribution being strongly athermal, the amplitude of excitation can be quantified by an equivalent excited electron temperature $T_{exc}\,(= T_0 + \Delta T_{exc})$, corresponding to the equilibrium temperature of an electron gas with the same total energy as the excited system (ΔT_{exc} commonly being in the 10–1000 K range). In the case of interband excitation ($\lambda_{pump} < \lambda_{ib}$), the total number of conduction electrons is no longer constant. Nevertheless, the interband electron-hole pairs recombine within a few tens of femtoseconds via Auger processes [96,97].

After excitation, the electron gas thermalizes through internal electron-electron interactions (second term in Eq. (13)). This process is described by a screened Coulomb interaction potential, containing a sum over all possible two-electron scattering processes satisfying energy and momentum conservation [6,22,98]. Although a direct single electron-electron scattering process is very fast (∼10 fs), a large number of them are required for establishing a thermalized electronic temperature. In the low perturbation regime, typical internal thermalization timescales of bulk materials and large nanoparticles are of the order of 500 fs and 350 fs for gold and silver respectively, and are shown to decrease for small nanoparticles ($D < 5$ nm), an effect ascribed to the reduction of Coulomb screening close to the surfaces [6,11,20].

Concomitantly with internal thermalization, the electron excess energy is transferred from the electron gas to the ionic lattice via electron-phonon scattering. The corresponding contribution (last term in Eq. (13)) is obtained by an integration of the e-ph coupling matrix element over all available electronic and vibrational states satisfying energy and momentum conservation [6,92]. As in the case of phonon-assisted photon absorption (τ_{e-ph}^{-1} term in Eq. (3)), a deformation potential coupling is assumed to compute the matrix element. The timescale for electron-lattice thermalization by electron-phonon scattering processes is typically in the picosecond range and depends on the excitation conditions [38]. In the low perturbation regime, it is longer in bulk gold (1.15 ps) than in silver (850 fs) and is also shown to decrease for small nanoparticles ($D < 20$ nm) [6,12]. It should be underlined that the Boltzmann equation (Eq. (13)), which was first introduced and applied to compute the dynamics of bulk materials, can still be used in a first approximation to describe the kinetics of not too small nanoparticles ($D > 2$–3 nm), provided a size-dependent correction to electron-electron and electron-phonon coupling rates is taken into account.

A simple description of electron gas and lattice dynamics after electron internal thermalization is given by the two temperature model (TTM), which assumes that both conduction electrons and lattice phonons are internally thermalized and their interaction strength is determined by a constant coupling term G [57,99–102]. Under these assumptions, T_e and T_L being the temperatures of internally thermalized electrons and lattice, respectively (considered homogeneous over the metal sample), and $C_e(T_e)$ and C_L their specific heats par unit volume, the following rate equation system applies:

$$\begin{aligned} C_e\left(T_e\right)\frac{\partial T_e}{\partial t} &= -G\left(T_e - T_L\right) \\ C_L\frac{\partial T_L}{\partial t} &= G\left(T_e - T_L\right) \end{aligned} \tag{14}$$

with $C_e(T_e) = aT_e$, and $a = 65$ J m^{-3} K^{-2} for Ag and Au [55]. This expression of C_e is valid in noble metals as long as electronic heating only involves quasi-free conduction band electrons, i.e., for not too strong excitation ($\Delta T_{exc} \leqslant 3000$ K). In this regime, the TTM equations (Eq. (14)) are a direct consequence of the Boltzmann equation (Eq. (13)), and are obtained by computing the electron energy loss rate in the thermalized regime [102].

Analytic solutions show that the final equilibrium temperature of the metal, common to the electron gas and the lattice, is given by $T_{eq} \approx T_0 + (T_{exc}^2 - T_0^2)/(2C_L/a)$, which is in general much smaller than T_{exc}, as $C_L \gg C_e$ (subsequent energy transfer to the environment is neglected here) [101]. For weak electron heating, i.e. $\Delta T_{exc} \ll T_0$, both electron and lattice temperatures exponentially converge to T_{eq}:

$$\begin{aligned} T_e\left(t\right) &\approx T_{eq} + \left(T_{exc} - T_{eq}\right)\,\exp\left(-\frac{t}{\tau_{e-L}}\right) \\ T_L\left(t\right) &\approx T_{eq} - \left(T_{eq} - T_0\right)\,\exp\left(-\frac{t}{\tau_{e-L}}\right) \end{aligned} \tag{15}$$

with a decay rate $\tau_{e-L}^{-1} \approx G/aT_0$ proportional to the electron-phonon coupling constant G. For stronger excitation, the T_e dependence of C_e leads to a non-exponential decay of T_e and to slowing down of the initial cooling dynamics, an exponential dependence being recovered when the electron gas cools down [101]. The excess energy density per unit volume of the electron gas $\Delta u_e(t) = a/2[T_e^2 - T_0^2]$ follows the T_e time-evolution, and similarly decreases with time after ultrafast excitation.

As the electron-lattice equilibrium temperature T_{eq} is higher than the one of the environment (T_0), energy is subsequently transferred to the external matrix through the nanoparticle interface [17,18,103]. The heat transfer out of the nanoparticles (typical timescale 10 to 500 ps, see Fig. 1c) is limited by the thermal resistance at the interface and by the thermal diffusion inside the matrix [17]. The relative contributions of these two effects depend on the size of the nanosystems, the effect of interfacial thermal resistance increasing with higher surface-to-volume ratios [18,103–106].

It should be noted that less computationally cumbersome numerical models are commonly used as an alternative to the approach presented here, i.e. the solution of equation (13) by calculations of all the Boltzmann equation terms. They are based on simplification of some interaction terms (e.g., the e–e one) with the use of a phenomenological description [107,108], or on an extension of the TTM taking into account non thermal electrons [109,110].

5 Time-dependent metal dielectric function change

The ultrafast optical response of a metal nanoparticle is ruled by the transient variations of its dielectric function $\Delta\varepsilon_{1,2}$. These are a consequence of the modification of the electron distribution, which induces a change in the interband term $\Delta\varepsilon_{1,2}^{ib}$ (dominant on the short timescale) and smaller modifications to the Drude term, and of the concomitant heating of the lattice (this effect being more significant on longer timescales).

5.1 Electronic contribution

Modifications Δf of electron occupation numbers (Eq. (13)) directly reflect into a change of interband dielectric function ε^{ib}. As in the case of the stationary absorption spectra, deduction of $\Delta\varepsilon_{1,2}^{ib}$ from Δf can be done using Au and Ag band structure models of Rosei [72] after integrating Δf over the joint density of states (Eqs. (6) and (7) and Tab. 1). The imaginary part $\Delta\varepsilon_2^{ib}(\lambda, t)$ is first computed as a function of the probe wavelength λ for each time delay t after pump excitation (corresponding to temperature increase ΔT_{exc}). The real part $\Delta\varepsilon_1^{ib}(\lambda, t)$ is subsequently deduced by Kramers-Kronig integral transformation (transient $\Delta\varepsilon_2(\lambda, t)$ in optical pump-probe experiments is different from zero only around the interband transition threshold, making integration possible). As an example, Δf for bulk Au is shown in the inset of Figure 4a for three different delays $t = 100$ fs, 500 fs and 3 ps after an initial 50 fs pump pulse at $\lambda_{pump} = 850$ nm and an equivalent electron temperature increase $\Delta T_{exc} = 100$ K. As expected, the pump pulse directly promotes electrons from occupied states with energy lower than the Fermi level to

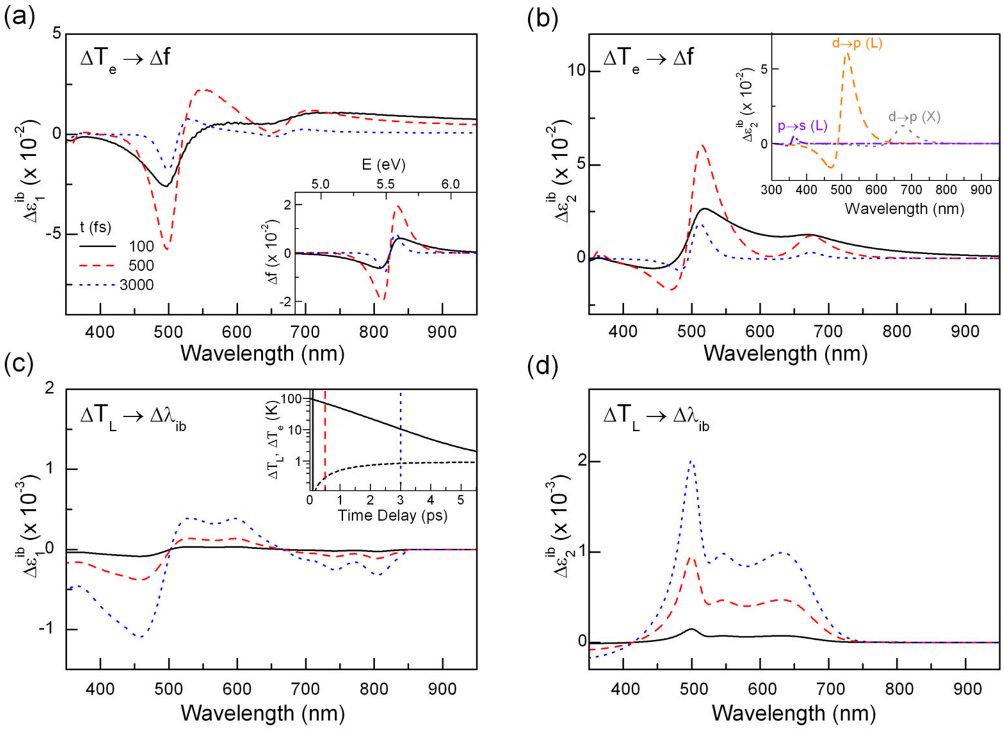

Fig. 4. Computed contributions to interband dielectric function changes, $\Delta\varepsilon_{1,2}^{ib}(\lambda, t)$, in Au following excitation by a 50 fs ultrafast pump pulse corresponding to an electron temperature increase $\Delta T_{exc} = 100$ K and $\lambda_{pump} = 850$ nm. Solid, dashed and dotted lines correspond to 100 fs, 500 fs and 3 ps delay after excitation, respectively. (a) and (b) show modifications due to electron heating (by changes of Δf), (c) and (d) the ones following lattice heating (by changes of the interband transition threshold). The inset in (a) reports the Δf distribution for the different delays. The three different interband transition contributions (Eq. (7)) to $\Delta\varepsilon_2^{ib}$ at 500 fs delay are separately plotted in the inset in (b). ΔT_e (equal to 94 K, 71 K and 11 K for 100 fs, 500 fs and 3 ps delay, respectively) and ΔT_L (0.06 K, 0.39 K and 0.82 K) computed by the TTM are reported in the inset of (c).

unoccupied states at energy hc/λ_{pump} above, modifying the occupation number of states in a broad energy band ranging from $E_F - hc/\lambda_{pump}$ to $E_F + hc/\lambda_{pump}$ (solid line in the inset Fig. 4a, corresponding to $t = 100$ fs). Fast internal thermalization progressively leads to build up of a narrower Δf distribution centered around E_F (dashed line, $t = 500$ fs). Afterwards, the electron energy loss by electron-phonon coupling induces a progressive vanishing of Δf (dotted line, $t = 3$ ps). The transient $\Delta\varepsilon_1^{ib}$ and $\Delta\varepsilon_2^{ib}$ spectra (Figs. 4a and 4b, respectively) reveal the gradual smearing out and narrowing of Δf around the Fermi energy. While they are flat for short delays, reflecting Δf broadening, they become sharper around the interband transition wavelengths during internal thermalization, before decreasing. Two main peaks are visible (Fig. 4b), corresponding to the $d \to p$ (X) and $d \to p$ (L) transitions (see inset of Fig. 4b), the L point giving, as expected, the largest contribution to the transient signal (Eq. (7) and Tab. 1).

Electron excitation also affects the Drude contribution to dielectric functions through a transient term $\Delta\varepsilon_{1,2}^{D}$. This is due to the dependence on the electron distribution (which depends in turn on temperature T_e) of the rate of all scattering processes (τ_n^{-1} in Eqs. (2) and (3)). As ε_1^D is almost independent of τ_n^{-1} (Eq. (2)), the only significant transient contribution originates from the imaginary part and is given by:

$$\Delta\varepsilon_2^D \approx \frac{\lambda^3}{2\pi c \lambda_p^2} \Delta\tau_n^{-1}. \tag{16}$$

Variations of τ_n^{-1} with electron temperature are dominated by the electron-electron scattering term $\Delta\tau_{e-e}^{-1}$, whose T_e dependence can be expressed as [59,102]:

$$\frac{\Delta\tau_{e-e}^{-1}}{\tau_{e-e}^{-1}}(\lambda, T_e) \approx \left(\frac{2\pi k_B \lambda}{hc}\right)^2 \left(T_e^2 - T_0^2\right). \tag{17}$$

For a weak excitation, the $\Delta\varepsilon_2^D$ contribution (Fig. 5a, with $\hbar\tau_{e-e}^{-1} \approx 15$ meV [56]) is small as compared to the variation of the interband dielectric function $\Delta\varepsilon_2^{ib}$ (Fig. 4b), while it becomes dominant for strong electron heating, due to the quadratic dependence of $\Delta\tau_{e-e}^{-1}$ on T_e (Eq. (17)).

The temperature dependence of the τ_{e-S}^{-1} contribution (Eqs. (3) and (4)) comes from the modification of the surface factor g (Eq. (5)) which is dominated by variations of electron occupation numbers Δf. Its influence on ε_2^D can be appreciable in the case of small nanoparticles, as shown in Figure 5b for 10 nm Au nanospheres. It can become more important for still smaller nano-objects, as shown for Ag nanospheres, bringing the first evidence of quantum confinement in their transient optical response [53].

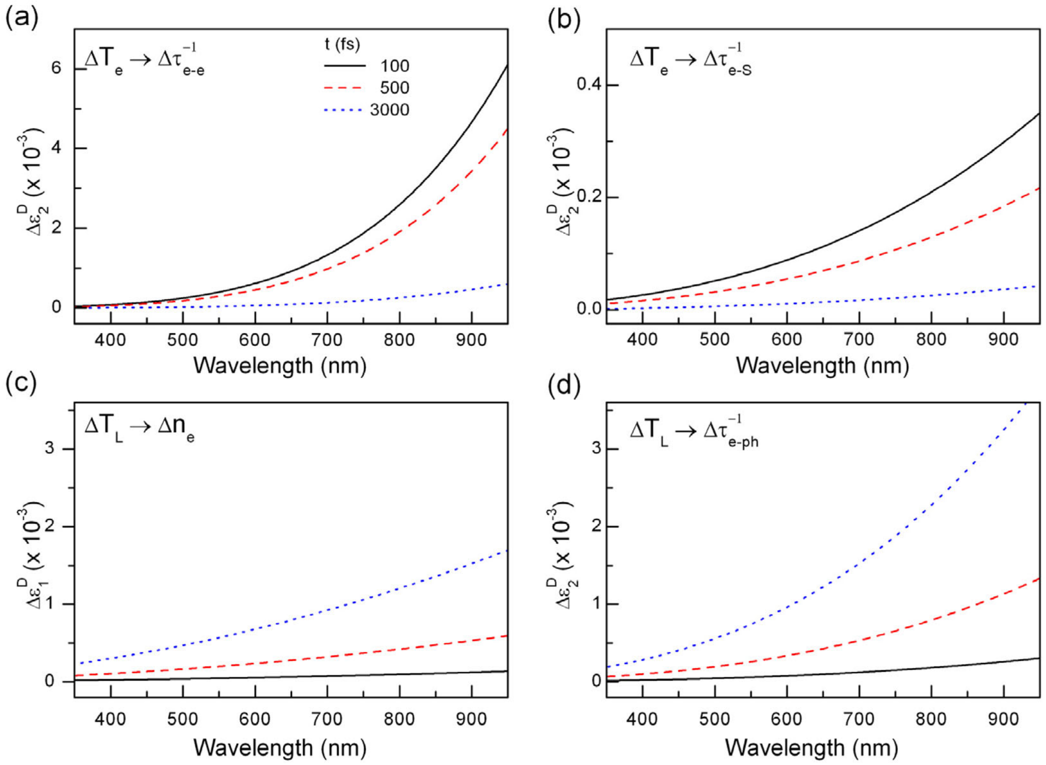

Fig. 5. Computed changes of the Drude contribution to the dielectric functions in Au following excitation in the same conditions as in Figures 4a and 4b. (a) and (b) show the effect on $\Delta\varepsilon_2^D$ of electron gas heating (by modifications of τ_{e-e}^{-1} and τ_{e-S}^{-1} for a 10 nm diameter gold nanoparticle, respectively), (c) and (d) the influence of lattice temperature (by modifications of n_e and τ_{e-ph}^{-1}, respectively).

5.2 Lattice contribution

After thermalization with the lattice (occurring within a few ps) the electron temperature has decreased to the new equilibrium value, $T_e = T_L = T_{eq} > T_0$, and the direct contribution of hot electron dynamics to the optical response becomes negligible. Nevertheless, the dielectric functions have not yet relaxed to the value before excitation, due to their sensitivity on the lattice temperature rise and the concomitant metal dilation, both decaying with cooling by energy transfer to the environment.

The increased equilibrium interatomic distance of the heated lattice leads to a modification of the electronic band structure, mainly due to a reduced overlap between orbitals, thus affecting band hybridization [67]. The filling of electronic energy bands and the position of the Fermi energy are modified accordingly. The effect on $\Delta\varepsilon_2^{ib}$ can be estimated through the different $\varepsilon_{2,l}^{ib}$ contributions (e.g. $d \rightarrow p$ around the L point, Fig. 2), by taking into account the displacement of individual interband transition thresholds $\lambda_{ib,l}$ with dilation under the assumption of a rigid band shift ($\partial\varepsilon_{2,l}^{ib}/\partial\lambda_{ib,l} = -\partial\varepsilon_{2,l}^{ib}/\partial\lambda$):

$$\Delta\varepsilon_2^{ib}(\lambda, t) = -\left(\sum_l \frac{\partial\varepsilon_{2,l}^{ib}}{\partial\lambda}\frac{\partial\lambda_{ib,l}}{\partial T_L}\right)\Delta T_L(t). \qquad (18)$$

The term $\partial\lambda_{ib,l}/\partial T_L$ is estimated starting from temperature-dependent ellipsometric measurements on bulk gold, which yield $\partial(\hbar\omega_{ib})/\partial T_L \approx -1.7 \times 10^{-4}$ and -3.2×10^{-4} eV/K for the d-band to Fermi energy transition around the L and X point, respectively [111] (the contribution of the transition from Fermi energy to s-band around the L point is smaller and its dependence on T_L is neglected here). The $\partial\varepsilon_{2,l}^{ib}/\partial\lambda$ derivatives are numerically deduced from the fit of the experimental bulk dielectric function (Fig. 2). In parallel, the $\Delta\varepsilon_1^{ib}$ contribution is estimated by derivation of the Johnson and Christy bulk experimental data after subtraction of the Drude part [102]. The estimated changes of $\Delta\varepsilon_{1,2}^{ib}$ (Figs. 4c and 4d) show some structures around the onset of interband transitions and their contribution increases with lattice temperature (the time dependence of electron and lattice temperatures computed with the TTM is shown in the inset of Fig. 4c).

Finally, lattice heating affects the $\varepsilon_{1,2}^D$ Drude terms by an increase with ΔT_L of both the electron-phonon scattering rate τ_{e-ph}^{-1} and the plasma wavelength $\lambda_p \propto 1/\sqrt{n_e}$, electron density n_e decreasing with T_L. The $\Delta\varepsilon_2^D$ term (Eq. (16)) is indeed dominated by the contribution of $\Delta\tau_{e-ph}^{-1}$, whose variation with ΔT_L can be expressed as $\Delta\tau_{e-ph}^{-1} = (\partial\tau_{e-ph}^{-1}/\partial T_L)\Delta T_L$, with $\partial(\hbar\tau_{e-ph}^{-1})/\partial T_L \approx 0.125$ meV/K for gold [112] (Fig. 5d). Conversely, the real component ε_1^D (Eq. (2), Fig. 5c) is primarily impacted by reduction of the plasma wavelength due to dilation of the nanoparticle and concomitant decrease of n_e. $\Delta\varepsilon_1^D$ can be written as a function of the linear dilation coefficient of

Table 2. Summary of main contributions to the change of the Au dielectric functions with electron and lattice heating. The physical parameters responsible for $\varepsilon_{1,2}$ variations are specified, with corresponding equations and figures.

Effect	Typical timescale	Physical parameter	Dielectric function	Equation	Figure	Amplitude
Electronic contribution						
Δf	<ps		ε_1^{ib}, ε_2^{ib}	(6), (7)	4a, 4b	dominant
ΔT_e	<ps	$\Delta\tau_{e-e}^{-1}$	ε_2^D	(16), (17)	5a	dominant
		$\Delta\tau_{e-S}^{-1}$	ε_2^D	(5), (16)	5b	size-dependent
		$\Delta\tau_{e-ph}^{-1}$	ε_2^D			negligible
Lattice contribution						
ΔT_L	>ps	$\Delta\lambda_{ib}$	ε_1^{ib}, ε_2^{ib}	(18)	4c, 4d	small
ΔT_L	>ps	Δn_e	ε_1^D	(19)	5c	dominant
		$\Delta\tau_{e-ph}^{-1}$	ε_2^D	(16)	5d	dominant
		$\Delta\tau_{e-ph}^{-1}$	ε_1^D			negligible
		Δn_e	ε_2^D			negligible

Au ($\alpha_L \approx 1.42 \times 10^{-5}$ K^{-1}):

$$\Delta\varepsilon_1^D = -\frac{\lambda^2}{\lambda_p^2}\frac{\Delta n_e}{n_e} = \frac{\lambda^2}{\lambda_p^2}3\alpha_L\Delta T_L. \qquad (19)$$

It should be noticed that volume change thus induces comparable modification of both the interband (electronic band shifting) and intraband (change of electronic density) contributions, the former showing mostly around the interband threshold λ_{ib}, the latter dominating in the red part of the spectrum (Figs. 4 and 5). These two mechanisms are fundamental for the optical detection of acoustic vibrations of nano-objects (inducing periodic volume changes) [5,7,15,39,43,113].

As expected, for a delay longer than ~1 ps (electron-lattice thermalization) the amplitudes of all contributions to ε proportional to the electronic temperature ΔT_e are decaying (Figs. 4a, 4b, 5a and 5b) while the ones depending on ΔT_L increase (Figs. 4c, 4d, 5c and 5d, see also Tab. 2 for a summary of all the contributions to $\Delta\varepsilon$). Interestingly, computation of $d\varepsilon_{1,2}/dT_L$ derivatives by summing interband (Eq. (18)) and Drude-like (Eq. (19)) contributions (Figs. 4c, 4d, 5c and 5d) shows good quantitative agreement with $d\varepsilon_{1,2}/dT_L$ derivatives (Fig. 6) deduced from recent measurements [114]. The estimated and measured wavelength dispersions are similar, the residual discrepancy in the absolute values of these derivatives being possibly due to uncertainties in the values of the parameters in the previous estimated contributions (e.g. Eq. (18)) [111] or to modifications not taken into account in this model, such as other changes of the electron band structure (e.g., slight change of electron effective mass [115]).

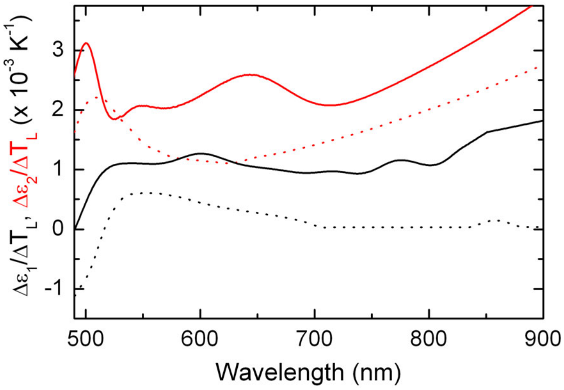

Fig. 6. Experimental (dotted lines) and theoretical (solid lines) determinations of ε_1 (black) and ε_2 (red) temperature dependence of Au. Experimental values are taken from reference [114], computed ones were obtained from the model described in Section 5.2 in the text.

5.3 Electronic and lattice contributions in Ag

The analysis of dynamical variations of $\Delta\varepsilon$ after ultrafast excitation can be extended to the case of Ag (Fig. 7). Δf dynamics (Eq. (13)) are very similar to those of gold (inset of Fig. 4a), the main difference being the faster electron internal and external thermalization in silver than in gold, as a consequence of the weaker contribution of the d-band electrons to screening in silver [6,20]. Transient variations $\Delta\varepsilon_{1,2}^{ib}$ of interband constants (Figs. 7a and 7b), computed with the Rosei model (Fig. 2) and parameters of Table 1, exhibit a large amplitude around 320 nm, corresponding to the onset of interband transitions around the L point of the Brillouin zone. Changes of interband constants with lattice heating (Eq. (18)) [116–118] are similar to the case of gold (not shown). Note that, due to very similar specific heats, the solution of the TTM (inset in Fig. 4c) gives a lattice temperature dependence almost identical for the two metals. Transient variations of the Drude terms are also similar. The $\Delta\varepsilon_1^D$ dependence on lattice temperature rise (Fig. 7c) is close to the one of Au (Eq. (19) with $\alpha_L \approx 1.89 \times 10^{-5}$ K^{-1} for Ag, Fig. 5c). Finally, $\Delta\varepsilon_2^D$ profiles (Fig. 7d) are dominated by the τ_{e-ph}^{-1} variation with lattice temperature ($\partial(\hbar\tau_{e-ph}^{-1})/\partial T_L \approx 0.057$ meV/K for

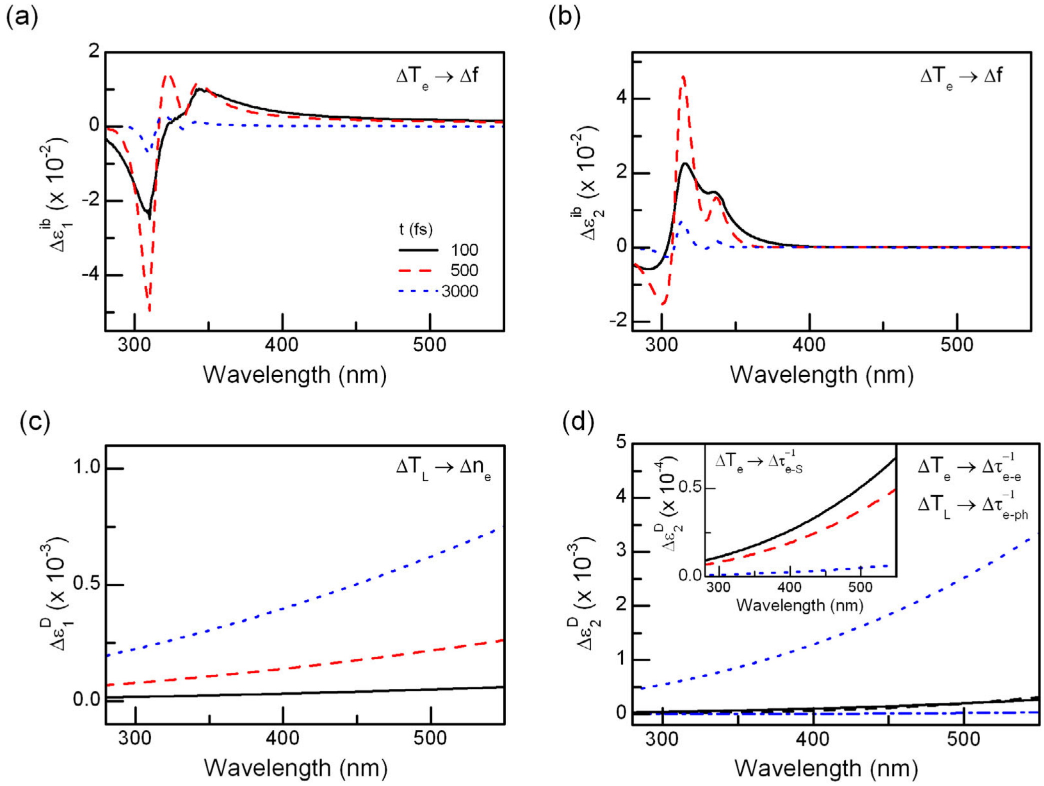

Fig. 7. Computed changes of interband and Drude dielectric functions in Ag following excitation by a 50 fs ultrafast pump pulse ($\Delta T_{exc} = 100$ K with $\lambda_{pump} = 850$ nm). Solid, dashed and dotted lines correspond to 100 fs, 500 fs and 3 ps delay after excitation, respectively. (a) and (b) show modifications due to electron heating, by changes of Δf. (c) shows the influence of lattice temperature on $\Delta\varepsilon_1^D$, by modifications of n_e. (d) shows the effect on $\Delta\varepsilon_2^D$ of lattice heating, by modifications of τ_{e-ph}^{-1} (solid and dotted lines corresponding to 100 fs and 3 ps), and the one of electron heating by modifications of τ_{e-e}^{-1} (dashed and dash-dotted lines corresponding to 100 fs and 3 ps). Inset shows $\Delta\varepsilon_2^D$ change dependent on τ_{e-S}^{-1} for 10 nm Ag nanospheres.

silver [112]), with a small contribution from the electron temperature dependent $\Delta\tau_{e-e}^{-1}$ (Eqs. (16) and (17) with $\hbar\tau_{e-e}^{-1} \approx 12$ meV [56]). Changes of τ_{e-S}^{-1} with temperature computed from the g dependence on Δf give the same profiles as for Au (inset of Fig. 7d).

6 Ultrafast nonlinear optical response of metal nanoparticles

Transient modifications of the extinction cross-section $\Delta\sigma_{ext}(\lambda, t)$ in the context of time-resolved experiments are computed using equation (1) by multiplying the nanoparticle $a_{1,2}$ (λ) derivative coefficients, determined from their linear absorption spectrum (Sect. 3, Fig. 3), and the Au and Ag $\Delta\varepsilon_{1,2}(\lambda, t)$ dielectric function changes (Sect. 5, Figs. 4, 5 and 7), taking into account both interband and intraband contributions (Fig. 8).

In the case of silver nanospheres (Fig. 8b), transient spectral features are centered around two distinct positions, namely λ_{SPR} (around 400 nm) and λ_{ib} (<320 nm). The former highlights the enhancement of the time-resolved response by plasmonic effects (large $a_{1,2}$ derivatives near SPR, Fig. 3b). The latter is similar to that of bulk silver [6] and reflects modification of the electron distribution around the Fermi energy and subsequent heating of the metal (Fig. 7). In the spectral region around λ_{ib}, $a_{1,2}$ are small and undispersed and the $\Delta\sigma_{ext}$ spectral shape reflects the dispersion of $\Delta\varepsilon_1$ and $\Delta\varepsilon_2$, determined by electron internal thermalization and cooling. As λ_{SPR} is spectrally separated from λ_{ib}, $\Delta\varepsilon_2^{ib}$ around the SPR is nonzero only for very short times t (<50 fs) and reflects a strongly out-of-equilibrium electron energy distribution during and immediately following excitation, with perturbation and probing of the occupation of electronic states energetically distant from Fermi level. For longer delays (~100 fs), this transient out-of-equilibrium contribution vanishes and $\Delta\sigma_{ext}$ becomes proportional to a_1. Its time behavior thus essentially follows that of $\Delta\varepsilon_1^{ib}$, which is approximately proportional to the electron excess energy density Δu_e [6,9]. As a result, far from interband transitions, $\Delta\sigma_{ext}$ increases with energy injection in the electrons and decays with the electron energy loss to the lattice. During electron-lattice thermalization, the spectral shape of $\Delta\sigma_{ext}$ is strongly modified. Interband $\Delta\varepsilon_{1,2}^{ib}$ contributions, which mainly depend on the electron temperature T_e, become negligible, and the strongest contributions come from the Drude term $\Delta\varepsilon_1^D$, proportional to lattice dilation, and $\Delta\varepsilon_2^D$, which reflects increase of the

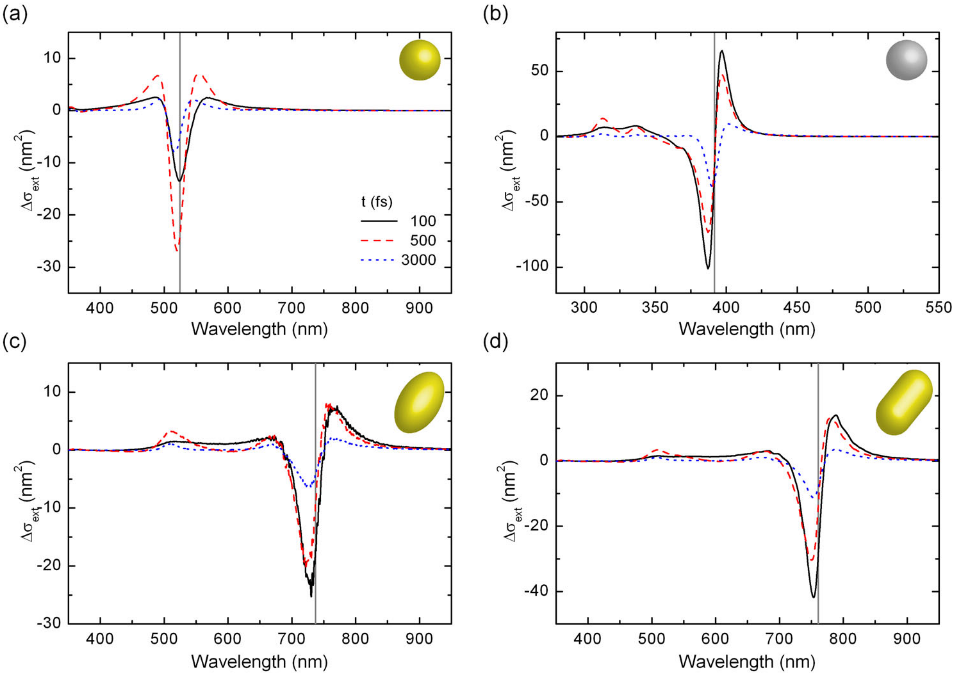

Fig. 8. Computed extinction cross-section changes for the same nanosystems as in Figure 3, for three different delays after excitation by a 50 fs ultrafast pump pulse ($\Delta T_{exc} = 100$ K with $\lambda_{pump} = 850$ nm), using equation (1) after determination of their spectral derivatives (Fig. 3) and dielectric functions changes (Figs. 4, 5 and 7). The vertical lines correspond to λ_{SPR} (see Fig. 3).

electron-phonon scattering rate (Figs. 7c and 7d). The latter being dominant, $\Delta\sigma_{ext}$ spectral shape reflects that of a_2.

In the case of a gold sphere, spectral overlap between plasmon resonance and interband transitions ($\lambda_{SPR} \approx \lambda_{ib}$, see Figs. 3 and 4) reflects for short delays in a specific spectral shape of the $\Delta\sigma_{ext}$ response, characterized by a profile with two zero crossings (Fig. 8a). For longer delays, as before, interband terms $\Delta\varepsilon_{1,2}^{ib}$ become negligible as compared to intraband ones and $\Delta\sigma_{ext}$ recovers a spectral dependence proportional to $a_2\Delta\varepsilon_2^D$. As the SPR position sensitively depends on aspect ratio, λ_{SPR} and λ_{ib} are separated on elongated gold nano-objects (Figs. 3c and 3d), in contrast to the gold nanosphere case. Calculations of $\Delta\sigma_{ext}$ for nanospheroids or nanorods, for a probe wavelength parallel to the major axis (Figs. 8c and 8d), illustrate this spectral separation between SPR and interband transition in the transient optical response, with distinct spectral features associated separately to $a_{1,2}$ derivative coefficients or dynamical modifications of dielectric constants $\Delta\varepsilon_{1,2}$, as in the case of a silver nanosphere (Fig. 8b).

7 Experiments on single metal nanoparticles and ensembles

Investigations on the transient optical response of single nano-objects are based on a pump-probe technique where two femtosecond laser beams are collinearly focused on the nanoparticle by a microscope objective (Fig. 1a). The first pulse (pump) excites the nanoparticle, whose time-resolved optical absorption is monitored by measuring the transmission change of the second delayed pulse (probe) with a photodiode. The experimentally measured relative differential transmission is connected to $\Delta\sigma_{ext}$ by [16,27,61]:

$$\frac{\Delta T}{T}(\lambda, t) = -\frac{\Delta\sigma_{ext}(\lambda, t)}{S} \tag{20}$$

where $T(\lambda, t)$ is the probe beam transmission and $S = (\pi D_{FWHM}^2)/(4\ln 2)$ the surface of the focused probe laser spot (D_{FWHM} being its full width at half maximum).

The first femtosecond investigation on a single metal nanoparticle was performed on isolated Ag nanospheres in the 20–40 nm size range [27], by combining the pump-probe experiment with Spatial Modulation Spectroscopy (SMS). This far-field technique permits single particle detection and quantitative determination of its linear extinction cross-section $\sigma_{ext}(\lambda)$ [82,119–121] (inset of Fig. 9b). Time-resolved pump-probe signals for different pump powers show a fast rise followed by a slower decay (Fig. 9a), corresponding to energy injection into the electron gas by the pump pulse and subsequent electron energy loss by thermalization with the lattice, respectively. Conversely to ensemble experiments, the nanoparticle excitation temperature for each of these measurements, ΔT_{exc}, can be precisely determined for the single optically characterized nano-object, as SMS provides the absolute value of its absorption cross-section at the experimental pump wavelength.

As described in Section 6, the ultrafast kinetics is mainly ruled by the time dependence of $\Delta\varepsilon_1^{ib}$, proportional to the electron excess energy $\Delta u_e(t)$ [6,9] for probe wavelengths far from the interband transition thresholds, as the $\Delta\varepsilon_2$ contribution is then negligible (Eq. (1)).

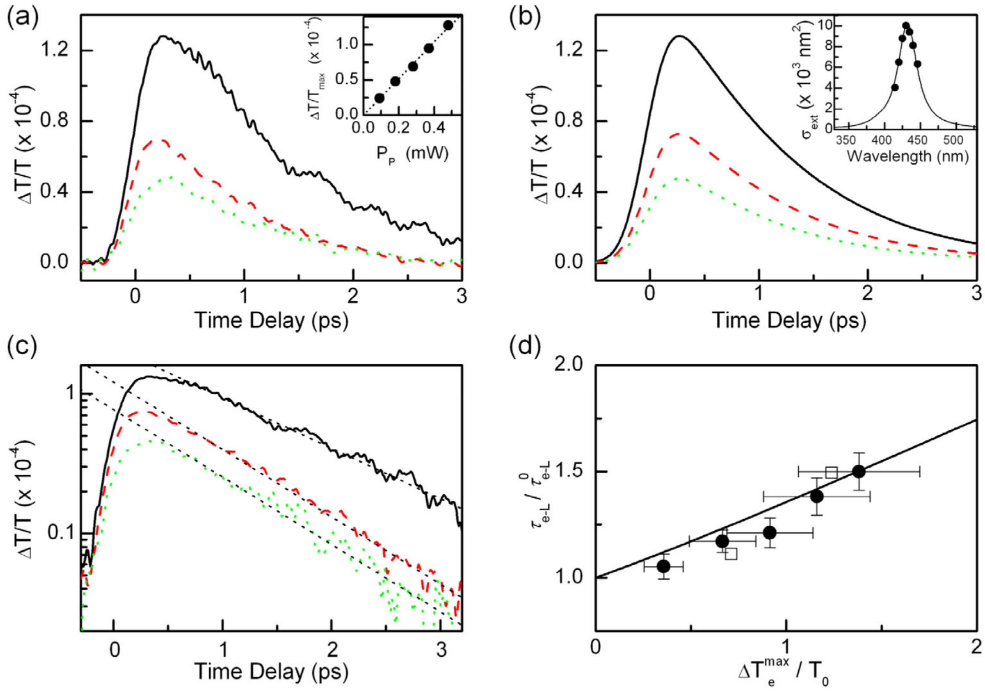

Fig. 9. (a) Time dependence of the transmission change $\Delta T/T$ measured for a single 30 nm Ag nanoparticle supported on a glass substrate, following excitation by a 140 fs pump pulse with $\lambda_{pump} = 850$ nm. Dotted, dashed and solid lines correspond to 180, 280 and 480 μW pump power, corresponding to $\Delta T_{exc} = 190$, 275 and 415 K, respectively. The inset shows the maximum of the $\Delta T/T$ signal as a function of pump power. (b) Simulated signals computed with equation (1), a_1 and a_2 derivatives being determined after fitting the measured extinction cross-section by Mie theory (shown in the inset). (c) Plots on logarithmic scale underline the change of decay time with excitation energy. (d) Normalized experimental decay times show good agreement with calculations based on TTM. Adapted from reference [27].

This reflects into a linear dependence of the amplitude of the time-resolved signals on excitation, as experimentally observed (inset in Fig. 9a). Computations based on the model described in Section 6 (solution of Boltzmann equation and modeling of optical changes), using the derivative coefficients computed from the linear experimental extinction cross-section and the dielectric function changes upon pump excitation, reproduce very well these pump power behaviors (Fig. 9b). For low excitations the decay dynamics is essentially monoexponential (Fig. 9c), the electron-phonon time constant τ_{e-L} increasing with excitation temperature ΔT_{exc}. A linear increase of τ_{e-L} with ΔT_{exc} is experimentally observed on single Ag nanospheres (Fig. 9d), in very good agreement with solution of the TTM (solid line in Fig. 9d) and with the numerical model.

In more recent pump-probe experiments on a single gold nanorod, the spectral shape, temporal dependence and absolute amplitude of its extinction cross-section change are found in excellent agreement with the dynamical model, thus allowing to quantitatively characterize the intrinsic optical nonlinearity of gold [32]. After its detection and quantitative linear absorption characterization by SMS, the ultrafast response of a single nanorod is measured in this experiment around $\lambda_{SPR} \approx 810$ nm (far from λ_{ib}) with probe polarization parallel to the major axis (Fig. 10). Simulations of the $\Delta\sigma_{ext}^{ib}$ dynamics, i.e. variations of $\Delta\sigma_{ext}$ induced by the interband term $\Delta\varepsilon_{1,2}^{ib}$ (see Sect. 6), reproduce very well the experiments, both for signal amplitude and time dependence (Figs. 10a and 10b) on the first picoseconds after excitation, justifying neglecting of the Drude term and of any lattice contribution to the short timescale signal. As expected, transient signals for short delays reflect the a_1 shape profile computed from the experimental linear σ_{ext} (Figs. 10c and 10d). This is because $\Delta\varepsilon_1^{ib}$ is approximately undispersed far from λ_{ib} and $\Delta\varepsilon_2^{ib}$ is small. For $\lambda \approx \lambda_{SPR}$ (black line in Figs. 10a and 10b), a_1 vanishes and $\Delta\sigma_{ext}$ reflects $\Delta\varepsilon_2^{ib}$ dynamics. Conversely, for longer delays ($t \approx 4$ ps), $\Delta\sigma_{ext}$ is not correctly reproduced any more by the $\Delta\varepsilon_{1,2}^{ib}$ terms alone, and inclusion of the $\Delta\varepsilon_2^{D}$ variation due to lattice heating becomes necessary (experiments and model prediction are represented by squares and dashed line in Fig. 10d, respectively). It should again be emphasized that preliminary determination of the nanorod absolute extinction cross-section σ_{ext} by SMS is the key here for quantitative modeling of the nanoparticle heating and of the corresponding modification to optical absorption. The transient response of the single nanorods can thus be precisely interpreted on the whole timescale as the combination of the dynamical response of the bulk metal (no corrections for size confinement were applied to determine gold nanorod $\Delta\varepsilon_{1,2}$) amplified by plasmonic effects [32].

In parallel with single particle investigations, the majority of pump-probe optical experiments have been performed on nanoparticle ensembles, either embedded in

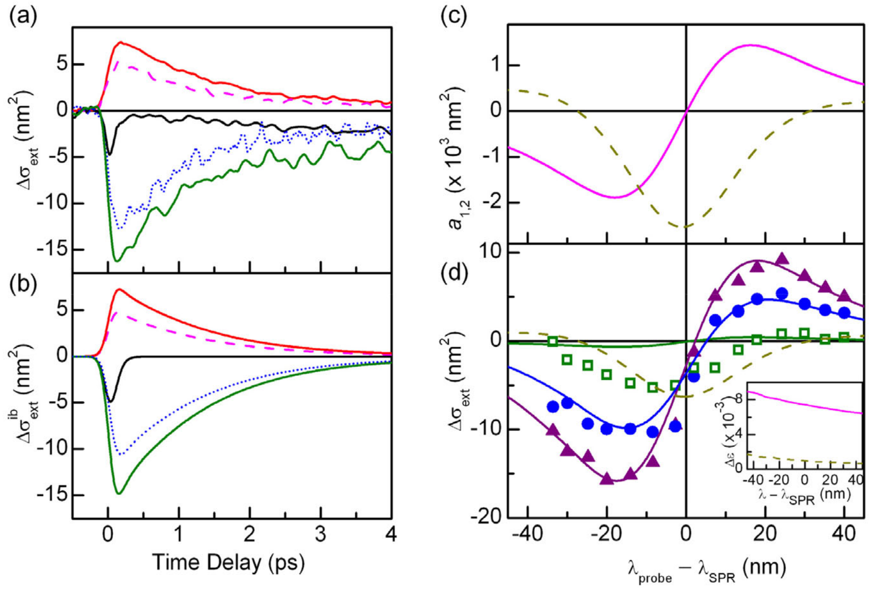

Fig. 10. (a) Ultrafast extinction cross-section changes $\Delta\sigma_{ext}$ measured for a single 43×12 nm Au nanorod after excitation with $\lambda_{pump} \approx 400$ nm and $\Delta T_{exc} = 125$ K at different probe wavelengths around its SPR: from top to bottom, $\lambda_{probe} - \lambda_{SPR} = +30$, $+40$, 0, –30 and –20 nm ($\lambda_{SPR} = 810$ nm). (b) Computed interband contributions (Eq. (1)). (c) a_1 and a_2 coefficients (solid and dashed lines, respectively) computed from the linear extinction cross-section. Vertical line corresponds to λ_{SPR}. (d) Dots, triangles and squares correspond to measured transient spectra for a delay of 0 fs, 200 fs and 4 ps, respectively. Full lines represent computed interband contributions for the same delays. Dashed line represents Drude contribution for the longest delay. The inset shows $\Delta\varepsilon_1^{ib}$ (solid line) and $\Delta\varepsilon_2^{ib}$ (dashed line) computed at $t = 200$ fs. Adapted from reference [32].

glass or dispersed in liquid (Fig. 1b). While they have the disadvantage of being less quantitative and being affected by inhomogeneous effects, investigations on ensembles are technically less demanding and easier to setup. By neglecting absorption by the matrix and restricting to small size and shape distributions and polarization-independent pump absorption (as for nanospheres or interband excitation of nanoellipsoids or nanorods, for example), the transmitted probe optical power can be expressed by $P_t(\lambda,t) = P_i \exp[-\alpha(\lambda,t)L]$, $\alpha(\lambda,t) = n_{np}\bar{\sigma}_{ext}(\lambda,t)$ being the absorption coefficient, with L the thickness of the sample (glass or cuvette), n_{np} the volume density of nanoparticles and $\bar{\sigma}_{ext}$ the mean value of their extinction cross-section. The experimental relative differential transmission can be expressed in this case by:

$$\frac{\Delta T}{T}(\lambda,t) = \frac{P_t(\lambda,t) - P_t(\lambda,0)}{P_t(\lambda,0)} \approx -\Delta\alpha(\lambda,t)L \approx -n_{np}L\Delta\bar{\sigma}_{ext}(\lambda,t). \tag{21}$$

It should be underlined that, as comparison of equations (20) and (21) highlights, quantitative determination of the absolute value of cross-section variations is more difficult in ensemble experiments, because of (1) inhomogeneous size and shape dispersion ($\Delta\bar{\sigma}_{ext}$ vs. $\Delta\sigma_{ext}$); (2) the density factor n_{np} which is in general not known with a good precision and (3) spatial extension of the pump and probe beams in the focal plane, generally leading to a non uniform heating and probing, respectively, within the intersection volume (this effect being neglected in Eq. (21), which applies to position-independent excitation and probing). Nonetheless, experiments on ensembles have brought deep insights into the dynamics of metal nano-objects.

In this context, early investigations on silver nanospheres [53] led to a physical interpretation of ultrafast SPR dynamics as a consequence of transient frequency shift and broadening of the SPR after excitation. Selective investigation of the SPR dynamics requires spectral separation of SPR and interband transitions, Ag nanospheres and Au nanorods both satisfying this condition, conversely to Au nanospheres (Fig. 3). As for individual nanorods, transient signals measured on ensembles of Ag nanoparticles in glass matrix around λ_{SPR} (Figs. 11a and 11b) show a dispersion-like transient profile, crossing the horizontal axis around λ_{SPR} and relaxing to the initial equilibrium value on a picosecond timescale. This specific derivative-type profile, with an increase of the sample absorption for wavelengths larger than the SPR, yields evidence for a pump-induced red-shift of the SPR, while its asymmetry indicates a concomitant broadening (Fig. 11b). These two effects could be isolated (Fig. 11c), and their different time dependences compared to the ones of $\Delta\varepsilon_{1,2}^{ib}$ (Fig. 11d).

As for the case of isolated gold nanorods, energy injection reflects into a fast increase of ε_1^{ib}, which directly translates into a red-shift of the SPR and decays to its initial value within a few ps by electron-lattice thermalization [53]. The SPR broadening has been shown to be determined by $\Delta\varepsilon_2$ containing two different contributions with different timescales: a fast one (50 fs) related again to the change of interband properties, $\Delta\varepsilon_2^{ib}$ reflecting ultrafast modifications of state occupation number during

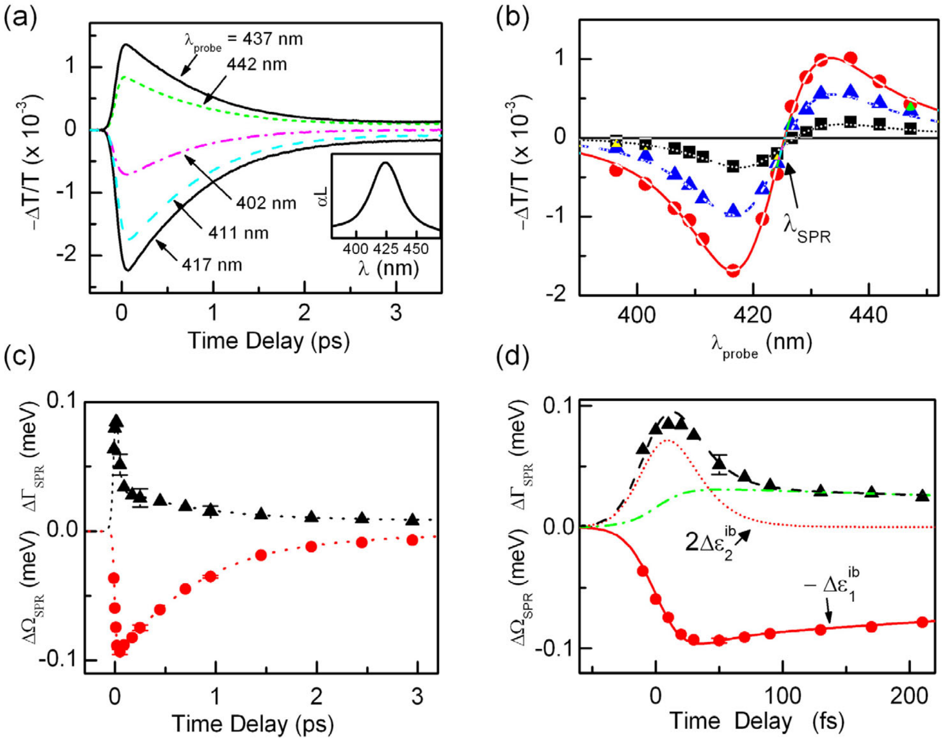

Fig. 11. (a) Measured time dependence of the relative absorption change $-\Delta T/T$ for different probe wavelengths in glass-embedded 26 nm diameter Ag nanoparticles. A 30 fs infrared pump pulse excitation was used, corresponding to an electron temperature increase $\Delta T_{exc} = 160$ K. The inset shows the sample absorption spectrum. (b) Probe wavelength dependence of the absorption change $-\Delta T/T$ around the SPR for probe delays of 400 fs (circles), 1 ps (triangles) and 2 ps (squares). Lines are fits assuming a pump-induced SPR frequency shift and broadening. (c) and (d) Measured time dependence of the SPR frequency shift ($\Delta\Omega_{SPR}$) and broadening ($\Delta\Gamma_{SPR}$). Full and dotted lines in (d) are the computed time-dependent $-\Delta\varepsilon_1^{ib}$ and $2\Delta\varepsilon_2^{ib}$. The dashed line is the estimated broadening, sum of the computed interband contribution (red dotted line) and an intraband one (dash-dotted). Adapted from reference [53].

and immediately after excitation, and a slower one due to changes of τ_n^{-1} (Eqs. (3) and (16)), the SPR width being proportional to the latter for a resonance spectrally separated from interband transitions [61]. The τ_n^{-1} dynamics is the sum of two weakly size-dependent terms (τ_{e-ph}^{-1} and τ_{e-e}^{-1}), which decay on a few ps timescale, and of the electron-surface scattering contribution (τ_{e-S}^{-1}) which is strongly size-dependent (Eq. (4)) and has a significant contribution on a shorter timescale (∼300 fs), when electron temperature is higher as hot electrons are not thermalized with the lattice yet. This surface induced effect is specific to confined systems, and becomes dominant in small nanoparticles, as evidenced by size-dependent investigations of the ultrafast dynamics of Ag nanoparticles with diameters varying from 30 nm to 6 nm (Fig. 12) [122]. It is a manifestation of quantum confinement, its experimental quantitative investigation being recently pursued by linear experiments on single nano-objects [61,62,65].

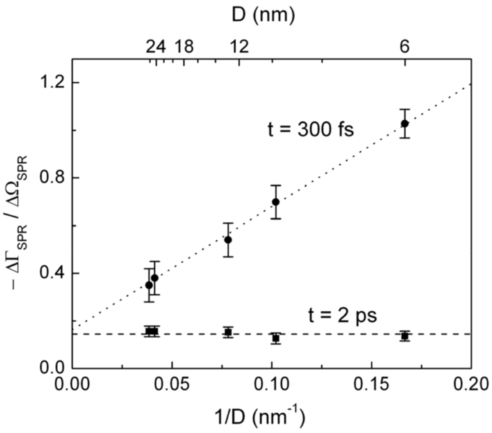

Fig. 12. Measured SPR broadening $\Delta\Gamma_{SPR}$ at a time delay of 300 fs (circles) and 2 ps (squares) normalized to the SPR shift $\Delta\Omega_{SPR}$ at 300 fs in glass-embedded Ag nanoparticles as a function of their inverse diameter (1/D), for an initial excitation corresponding to $\Delta T_{exc} = 250$ K. Adapted from reference [122].

In a slightly different context, the sensitivity of the SPR to thermal heating and electron density variations has been recently exploited to elucidate femtosecond charge transfer dynamics in hybrid semiconductor-metal nanosystems, composed by a Au sphere directly grown on the tip of a CdS nanorod [123,124]. Ultrafast pumping at 400 nm, resonant with CdS excitonic absorption (blue arrow in Fig. 13a), leads to photoexcitation of an electron into the semiconductor valence band, the electron being subsequently transferred to the Au sphere. After

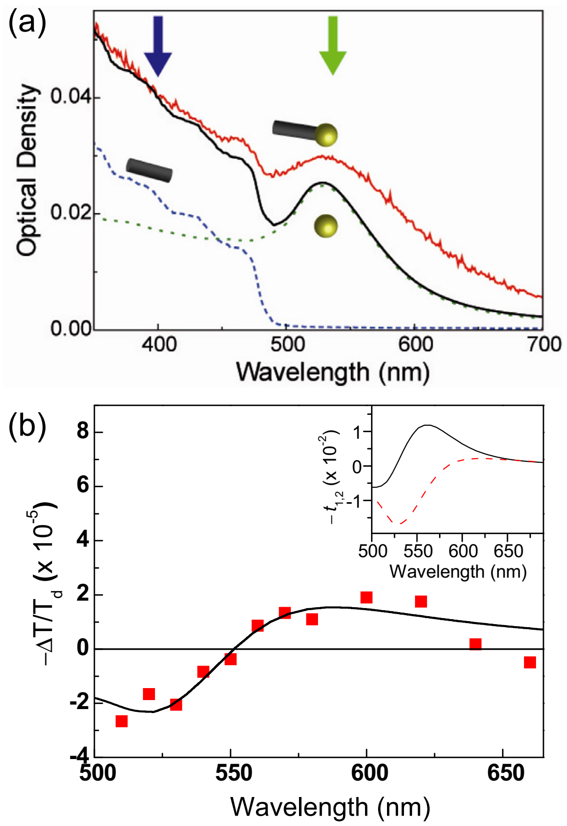

Fig. 13. (a) Experimental absorption spectrum of Au-CdS metal-semiconductor hybrid nano-objects in solution (solid red line). The distinct contributions to absorption of CdS (blue dashed line) and gold (green dotted line) demonstrate spectral separation between the semiconductor exciton (around 480 nm) and Au SPR (540 nm), solid black line being the sum of the two individual spectra. (b) Experimental spectral dependence of the absorption changes $-(\Delta T/T)_d$ for a 5 ps time delay (squares) and the corresponding fit (solid line) taking into account the semiconductor to metal electron and energy transfer and the subsequent n_e and τ_n^{-1} variations. The inset shows the derivatives t_1 (solid line) and t_2 (dashed line) of the transmission with respect to $\varepsilon_{1,2}$ used in the model. Adapted from reference [123].

fast electron-phonon thermalization (∼1 ps), the $\Delta T/T$ signal still presents a long-time component [123], signature of intraband modifications due to electron temperature and density changes. This is dominated for a delay of 5 ps by a SPR transient red-shift, characterized by an absorption decrease (increase) at $\lambda < \lambda_{SPR}$ ($\lambda > \lambda_{SPR}$), and an additional broadening (Fig. 13b). A fit of the transient signal (solid line) allows to determine the most significant contributions to the absorption change, $\Delta\lambda_p$ and $\Delta\tau_n^{-1}$, which are responsible for red-shift and broadening, through modifications of intraband ε_1^D and ε_2^D Drude terms, respectively (Eqs. (2) and (16)). As λ_p depends on electron density $n_e = N_e/V$, the fit of the transient red-shift allowed to determine a negative value for the density change $\Delta n_e/n_e = -(5 \pm 1) \times 10^{-5}$, which corresponds to a reduction of the electron density in the Au sphere induced by the addition of the supplementary photoexcited electron. Albeit surprising, this conclusion is in agreement with results on silver clusters in gas phase [125] and is quantitatively explained by the enhancement of the electronic occupied volume (induced by enhanced Coulomb repulsion, increasing the spill-out effect), which is stronger than the effect of electron number increment. In addition, a relative change $\Delta\tau_n^{-1}/\tau_n^{-1} = (1.1 \pm 0.5) \times 10^{-3}$ is obtained by the analysis of the time-resolved signals, this value being in excellent quantitative agreement with the τ_{e-ph}^{-1} electron-lattice scattering increase [112] corresponding to lattice heating after hot electron injection. These investigations are an example of ultrafast charge and energy transfer characterization by using the metal nanoparticle transient optical signal as probe for the electron dynamics.

8 Conclusion

We reviewed investigations on the nonlinear ultrafast optical response of metal nanosystems, performed both on ensembles of nanoparticles (embedded in a glass or immersed in a solution) and on single nano-objects. In order to quantitatively understand their ultrafast optical time-resolved response, a detailed theoretical model has been discussed. It predicts both the physical evolution of the nanosystems, after an initial out-of-equilibrium excitation, taking into account both electron and lattice heating and their thermalization, and the concomitant ultrafast changes of the nano-object metal dielectric functions, which is at the origin of the transient optical response. The different interband and intraband contributions to the modification of the dielectric functions have been discussed and the specific effects of electron and lattice dynamics on each contribution have been analyzed. We also detailed the crucial role of the metal nanoparticle localized surface plasmon resonance to the enhancement of the ultrafast optical response. Interestingly, both in the case of single gold nanorods and silver nanospheres, the transient optical response is shown to be obtained by the combination of the dynamical response of the bulk metal amplified by plasmonic effects, typical of nanometric confined systems, these experiments allowing to quantitatively determine intrinsic ultrafast nonlinearities of bulk materials.

An accurate modeling of the ultrafast response of metal nanoparticles opens the way to precisely understand subtle effects leading to small transient optical response changes. This is illustrated in the case of semiconductor to metal charge and energy transfer in hybrid nanosystems. In this situation, the analysis of the time- and wavelength-dependent transient optical spectra led to the determination of the number of electrons being transferred and to their dynamics [123]. More generally, fine analysis of the ultrafast optical response in metal nanosystems opens up many possibilities for the dynamical investigation of different physical processes, including electron and lattice dynamical coupling, acoustic and thermal kinetics, internal energy redistribution and energy transfer to the environment.

References

1. U. Kreibig, M. Vollmer, *Optical Properties of Metal Clusters* (Springer, Berlin, 1995)
2. K. Kelly, E. Coronado, L. Zhao, G. Schatz, J. Phys. Chem. B **107**, 668 (2003)
3. L.M. Liz-Marzán, Langmuir **22**, 32 (2006)
4. V. Myroshnychenko, J. Rodríguez-Fernández, I. Pastoriza-Santos, A.M. Funston, C. Novo, P. Mulvaney, L.M. Liz-Marzán, F.J. García de Abajo, Chem. Soc. Rev. **37**, 1792 (2008)
5. A. Crut, P. Maioli, N. Del Fatti, F. Vallée, Chem. Soc. Rev. **43**, 3921 (2014)
6. N. Del Fatti, C. Voisin, M. Achermann, S. Tzortzakis, D. Christofilos, F. Vallée, Phys. Rev. B **61**, 16956 (2000)
7. C. Voisin, N. Del Fatti, D. Christofilos, F. Vallée, J. Phys. Chem. B **105**, 2264 (2001)
8. M. Nisoli, S. Stagira, S. De Silvestri, A. Stella, P. Tognini, P. Cheyssac, R. Kofman, Phys. Rev. Lett. **78**, 3575 (1997)
9. N. Del Fatti, R. Bouffanais, F. Vallée, C. Flytzanis, Phys. Rev. Lett. **81**, 922 (1998)
10. V. Halté, J.-Y. Bigot, B. Palpant, M. Broyer, B. Prével, A. Pérez, Appl. Phys. Lett. **75**, 3799 (1999)
11. C. Voisin, D. Christofilos, N. Del Fatti, F. Vallée, B. Prével, E. Cottancin, J. Lermé, M. Pellarin, M. Broyer, Phys. Rev. Lett. **85**, 2200 (2000)
12. A. Arbouet, C. Voisin, D. Christofilos, P. Langot, N. Del Fatti, F. Vallée, J. Lermé, G. Celep, E. Cottancin, M. Gaudry, M. Pellarin, M. Broyer, M. Maillard, M.P. Pileni, M. Treguer, Phys. Rev. Lett. **90**, 177401 (2003)
13. N. Del Fatti, C. Voisin, D. Christofilos, F. Vallée, C. Flytzanis, J. Phys. Chem. A **104**, 4321 (2000)
14. A. Crut, P. Maioli, N. Del Fatti, F. Vallée, Phys. Chem. Chem. Phys. **11**, 5882 (2009)
15. G.V. Hartland, Chem. Rev. **111**, 3858 (2011)
16. A. Crut, P. Maioli, N. Del Fatti, F. Vallée, Ultrasonics, `DOI:10.1016/j.ultras.2014.02.013` (2014)
17. D.G. Cahill, W.K. Ford, K.E. Goodson, G.D. Mahan, A. Majumdar, H.J. Maris, R. Merlin, S.R. Phillpot, J. Appl. Phys. **93**, 793 (2003)
18. V. Juvé, M. Scardamaglia, P. Maioli, A. Crut, S. Merabia, L. Joly, N. Del Fatti, F. Vallée, Phys. Rev. B **80**, 195406 (2009)
19. J. Huang, J. Park, W. Wang, C.J. Murphy, D.G. Cahill, ACS Nano **7**, 589 (2013)
20. C. Voisin, D. Christofilos, P. Loukakos, N. Del Fatti, F. Vallée, J. Lermé, M. Gaudry, E. Cottancin, M. Pellarin, M. Broyer, Phys. Rev. B **69**, 195416 (2004)
21. J. Fujimoto, J. Liu, E. Ippen, N. Bloembergen, Phys. Rev. Lett. **53**, 1837 (1984)
22. C.-K. Sun, F. Vallée, L. Acioli, E. Ippen, J. Fujimoto, Phys. Rev. B **50**, 15337 (1994)
23. S. Link, M.A. El-Sayed, J. Phys. Chem. B **103**, 8410 (1999)
24. N. Del Fatti, F. Vallée, Appl. Phys. B **73**, 383 (2001)
25. M. Kiel, H. Möhwald, M. Bargheer, Phys. Rev. B **84**, 165121 (2011)
26. M. van Dijk, M. Lippitz, M. Orrit, Phys. Rev. Lett. **95**, 267406 (2005)
27. O.L. Muskens, N. Del Fatti, F. Vallée, Nano Lett. **6**, 552 (2006)
28. H. Staleva, G.V. Hartland, J. Phys. Chem. C **112**, 7535 (2008)
29. J. Burgin, P. Langot, N. Del Fatti, F. Vallée, W. Huang, M.A. El-Sayed, J. Phys. Chem. C **112**, 11231 (2008)
30. H. Baida, D. Christofilos, P. Maioli, A. Crut, N. Del Fatti, F. Vallée, J. Raman Spectrosc. **42**, 1891 (2011)
31. P.V. Ruijgrok, P. Zijlstra, A.L. Tchebotareva, M. Orrit, Nano Lett. **12**, 1063 (2012)
32. H. Baida, D. Mongin, D. Christofilos, G. Bachelier, A. Crut, P. Maioli, N. Del Fatti, F. Vallée, Phys. Rev. Lett. **107**, 057402 (2011)
33. F. Masia, W. Langbein, P. Borri, Phys. Rev. B **85**, 235403 (2012)
34. F. Masia, W. Langbein, P. Borri, Phys. Chem. Chem. Phys. **15**, 4226 (2013)
35. C. Guillon, P. Langot, N. Del Fatti, F. Vallée, New J. Phys. **5**, 13 (2003)
36. B. Lamprecht, J.R. Krenn, A. Leitner, F.R. Aussenegg, Phys. Rev. Lett. **83**, 4421 (1999)
37. A. Anderson, K.S. Deryckx, X.G. Xu, G. Steinmeyer, M.B. Raschke, Nano Lett. **10**, 2519 (2010)
38. J.H. Hodak, A. Henglein, G.V. Hartland, J. Phys. Chem. B **104**, 5053 (2000)
39. N. Del Fatti, C. Voisin, F. Chevy, F. Vallée, C. Flytzanis, J. Chem. Phys. **110**, 11484 (1999)
40. J.H. Hodak, A. Henglein, G.V. Hartland, J. Chem. Phys. **111**, 8613 (1999)
41. C. Voisin, D. Christofilos, N. Del Fatti, F. Vallée, Physica B **316-317**, 89 (2002)
42. Z. Ge, D.G. Cahill, P.V. Braun, J. Phys. Chem. B **108**, 18870 (2004)
43. A.L. Tchebotareva, P.V. Ruijgrok, P. Zijlstra, M. Orrit, Laser Photonics Rev. **4**, 581 (2010)
44. C. Guillon, P. Langot, N. Del Fatti, F. Vallée, A.S. Kirakosyan, T.V. Shahbazyan, T. Cardinal, M. Treguer, Nano Lett. **7**, 138 (2007)
45. V. Juvé, A. Crut, P. Maioli, M. Pellarin, M. Broyer, N. Del Fatti, F. Vallée, Nano Lett. **10**, 1853 (2010)
46. H.E. Sauceda, D. Mongin, P. Maioli, A. Crut, M. Pellarin, N. Del Fatti, F. Vallée, I.L. Garzón, J. Phys. Chem. C **116**, 25147 (2012)
47. T.A. Major, S.S. Lo, K. Yu, G.V. Hartland, J. Phys. Chem. Lett. **5**, 866 (2014)
48. C. Voisin, N. Del Fatti, D. Christofilos, F. Vallée, Appl. Surf. Sci. **164**, 131 (2000)
49. A. Gambetta, C. Manzoni, E. Menna, M. Meneghetti, G. Cerullo, G. Lanzani, S. Tretiak, A. Piryatinski, A. Saxena, R.L. Martin, A.R. Bishop, Nat. Phys. **2**, 515 (2006)
50. M. Pelton, J.E. Sader, J. Burgin, M. Liu, P. Guyot-Sionnest, D. Gosztola, Nat. Nanotechnol. **4**, 492 (2009)
51. T.A. Major, A. Crut, B. Gao, S.S. Lo, N. Del Fatti, F. Vallée, G.V. Hartland, Phys. Chem. Chem. Phys. **15**, 4169 (2013)
52. M. Pelton, D. Chakraborty, E. Malachosky, P. Guyot-Sionnest, J.E. Sader, Phys. Rev. Lett. **111**, 244502 (2013)
53. N. Del Fatti, F. Vallée, C. Flytzanis, Y. Hamanaka, A. Nakamura, Chem. Phys. **251**, 215 (2000)
54. C.F. Bohren, D.R. Huffman, *Absorption and Scattering of Light by Small Particles* (Wiley, New York, 1983)
55. N.W. Ashcroft, N.D. Mermin, *Solid State Physics* (Holt, Rinehart and Winston, New York, 1976)
56. J. Smith, H. Ehrenreich, Phys. Rev. B **25**, 923 (1982)

57. P.B. Allen, Phys. Rev. Lett. **59**, 1460 (1987)
58. C.-Y. Tsai, C.-H. Chen, T.-L. Sung, T.-Y. Wu, F.-P. Shih, IEEE J. Quantum Electron. **34**, 552 (1998)
59. R.N. Gurzhi, Sov. Phys. J. Exp. Theor. Phys. **35**, 673 (1959)
60. A. Kawabata, R. Kubo, J. Phys. Soc. Jpn **21**, 1765 (1966)
61. H. Baida, P. Billaud, S. Marhaba, D. Christofilos, E. Cottancin, A. Crut, J. Lermé, P. Maioli, M. Pellarin, M. Broyer, N. Del Fatti, F. Vallée, A. Sánchez-Iglesias, I. Pastoriza-Santos, L.M. Liz-Marzán, Nano Lett. **9**, 3463 (2009)
62. V. Juvé, M.F. Cardinal, A. Lombardi, A. Crut, P. Maioli, J. Pérez-Juste, L.M. Liz-Marzán, N. Del Fatti, F. Vallée, Nano Lett. **13**, 2234 (2013)
63. E.A. Coronado, G.C. Schatz, J. Chem. Phys. **119**, 3926 (2003)
64. F. Hache, D. Ricard, C. Flytzanis, J. Opt. Soc. Am. B **3**, 1647 (1986)
65. J. Lermé, H. Baida, C. Bonnet, M. Broyer, E. Cottancin, A. Crut, P. Maioli, N. Del Fatti, F. Vallée, M. Pellarin, J. Phys. Chem. Lett. **1**, 2922 (2010)
66. J. Lermé, J. Phys. Chem. C **115**, 14098 (2011)
67. N.E. Christensen, B.O. Seraphin, Phys. Rev. B **4**, 3321 (1971)
68. N.E. Christensen, Phys. Stat. Sol. B **54**, 551 (1972)
69. F. Bassani, G. Pastori-Parravicini, *Electronic States and Optical Transitions in Solids* (Pergamon Press, New York, 1975)
70. M. Dressel, G. Grüner, *Electrodynamics of Solids: Optical Properties of Electrons in Matter* (Cambridge University Press, Cambridge, New York, 2002)
71. H. Ehrenreich, M. Cohen, Phys. Rev. **115**, 786 (1959)
72. R. Rosei, Phys. Rev. B **10**, 474 (1974)
73. M. Guerrisi, R. Rosei, P. Winsemius, Phys. Rev. B **12**, 557 (1975)
74. R. Rosei, C. Culp, J. Weaver, Phys. Rev. B **10**, 484 (1974)
75. N.N. Smith, Phys. Rev. B **3**, 1862 (1971)
76. P.B. Johnson, R.W. Christy, Phys. Rev. B **6**, 4370 (1972)
77. J.H. Weaver, H.P.R. Frederikse, *CRC Handbook of Chemistry and Physics* (CRC Press, 1977)
78. N.P. Blanchard, C. Smith, D.S. Martin, D.J. Hayton, T.E. Jenkins, P. Weightman, Phys. Stat. Sol. C **0**, 2931 (2003)
79. R.L. Olmon, B. Slovick, T.W. Johnson, D. Shelton, S.-H. Oh, G.D. Boreman, M.B. Raschke, Phys. Rev. B **86**, 235147 (2012)
80. T. Rangel, D. Kecik, P.E. Trevisanutto, G.-M. Rignanese, H. Van Swygenhoven, V. Olevano, Phys. Rev. B **86**, 125125 (2012)
81. E.D. Palik, *Handbook of Optical Constants of Solids* (Academic Press, Orlando, 1985)
82. P. Billaud, J.R. Huntzinger, E. Cottancin, J. Lermé, M. Pellarin, L. Arnaud, M. Broyer, N. Del Fatti, F. Vallée, Eur. Phys. J. D **43**, 271 (2007)
83. F. Vallée, in *Nanomaterials and Nanochemistry*, edited by C. Bréchignac, P. Houdy, M. Lahmani (Springer-Verlag, Heidelberg, 2007), pp. 197–228
84. H. Hövel, S. Fritz, A. Hilger, U. Kreibig, M. Vollmer, Phys. Rev. B **48**, 18178 (1993)
85. J. Pérez-Juste, I. Pastoriza-Santos, L.M. Liz-Marzán, P. Mulvaney, Coord. Chem. Rev. **249**, 1870 (2005)
86. O.L. Muskens, G. Bachelier, N. Del Fatti, F. Vallée, A. Brioude, X. Jiang, M.-P. Pileni, J. Phys. Chem. C **112**, 8917 (2008)
87. C. Sönnichsen, T. Franzl, T. Wilk, G. von Plessen, J. Feldmann, Phys. Rev. Lett. **88**, 077402 (2002)
88. Y.R. Davletshin, A. Lombardi, M.F. Cardinal, V. Juvé, A. Crut, P. Maioli, L.M. Liz-Marzán, F. Vallée, N. Del Fatti, J.C. Kumaradas, ACS Nano **6**, 8183 (2012)
89. A. Lombardi, M. Loumaigne, A. Crut, P. Maioli, N. Del Fatti, F. Vallée, M. Spuch-Calvar, J. Burgin, J. Majimel, M. Tréguer-Delapierre, Langmuir **28**, 9027 (2012)
90. N.V. Voshchinnikov, V.G. Farafonov, Astrophys. Space Sci. **204**, 19 (1992)
91. J. Jin, *The Finite Element Method in Electromagnetics*, 2nd edn. (John Wiley & Sons, New York, 2002)
92. J.M. Ziman, *Principles of the Theory of Solids* (Cambridge University Press, Cambridge, 1969)
93. P.E. Hopkins, J.L. Kassebaum, P.M. Norris, J. Appl. Phys. **105**, 023710 (2009)
94. L. Guo, S.L. Hodson, T.S. Fisher, X. Xu, J. Heat Transfer **134**, 042402 (2012)
95. S. Park, M. Pelton, M. Liu, P. Guyot-Sionnest, N.F. Scherer, J. Phys. Chem. C **111**, 116 (2007)
96. E. Knoesel, A. Hotzel, M. Wolf, Phys. Rev. B **57**, 12812 (1998)
97. R. Matzdorf, A. Gerlach, F. Theilmann, G. Meister, A. Goldmann, Appl. Phys. B **68**, 393 (1999)
98. P. Nozieres, D. Pines, *Theory of Quantum Liquids* (W.A. Benjamin, 1966)
99. M.I. Kaganov, I.M. Lifshitz, L.V. Tanatarov, Sov. Phys. J. Exp. Theor. Phys. **4**, 173 (1957)
100. S.I. Anisimov, B.L. Kapeliovich, T.L. Perel'man, Sov. Phys. J. Exp. Theor. Phys. **39**, 375 (1974)
101. N. Del Fatti, A. Arbouet, F. Vallée, Appl. Phys. B **84**, 175 (2006)
102. F. Vallée, N. Del Fatti, in *Challenges and Advances in Computational Chemistry and Physics*, edited by T. Shahbazyan, M. Stockman (Springer, 2013), pp. 167–205
103. M. Hu, G.V. Hartland, J. Phys. Chem. B **106**, 7029 (2002)
104. O. Wilson, X. Hu, D. Cahill, P. Braun, Phys. Rev. B **66**, 224301 (2002)
105. F. Banfi, V. Juvé, D. Nardi, S. Dal Conte, C. Giannetti, G. Ferrini, N. Del Fatti, F. Vallée, Appl. Phys. Lett. **100**, 011902 (2012)
106. A. Plech, V. Kotaidis, S. Grésillon, C. Dahmen, G. von Plessen, Phys. Rev. B **70**, 195423 (2004)
107. B. Palpant, Y. Guillet, M. Rashidi-Huyeh, D. Prot, Gold Bull. **41**, 105 (2008)
108. Y. Guillet, M. Rashidi-Huyeh, B. Palpant, Phys. Rev. B **79**, 045410 (2009)
109. G. Della Valle, M. Conforti, S. Longhi, G. Cerullo, D. Brida, Phys. Rev. B **86**, 155139 (2012)
110. E. Carpene, Phys. Rev. B **74**, 024301 (2006)
111. P. Winsemius, M. Guerrisi, R. Rosei, Phys. Rev. B **12**, 4570 (1975)
112. G. Parkins, W. Lawrence, R. Christy, Phys. Rev. B **23**, 6408 (1981)
113. M. Hu, X. Wang, G.V. Hartland, P. Mulvaney, J. Perez-Juste, J.E. Sader, J. Am. Chem. Soc. **125**, 14925 (2003)
114. R.B. Wilson, B.A. Apgar, L.W. Martin, D.G. Cahill, Opt. Exp. **20**, 28829 (2012)
115. M. Rashidi-Huyeh, B. Palpant, Phys. Rev. B **74**, 075405 (2006)

116. P. Winsemius, F.F. van Kampen, H.P. Lengkeek, C.G. van Went, J. Phys. F **6**, 1583 (1976)
117. M. Rashidi Huyeh, M. Shirdel Havar, B. Palpant, J. Appl. Phys. **112**, 103101 (2012)
118. F. Antonangeli, E. Colavita, R. Rosei, S.E. Salusti, Nuovo Cimento B **24**, 121 (1974)
119. A. Arbouet, D. Christofilos, N. Del Fatti, F. Vallée, J.R. Huntzinger, L. Arnaud, P. Billaud, M. Broyer, Phys. Rev. Lett. **93**, 127401 (2004)
120. O.L. Muskens, D. Christofilos, N. Del Fatti, F. Vallée, J. Opt. A **8**, S264 (2006)
121. O.L. Muskens, P. Billaud, M. Broyer, N. Del Fatti, F. Vallée, Phys. Rev. B **78**, 205410 (2008)
122. N. Del Fatti, C. Flytzanis, F. Vallée, Appl. Phys. B **68**, 433 (1999)
123. D. Mongin, E. Shaviv, P. Maioli, A. Crut, U. Banin, N. Del Fatti, F. Vallée, ACS Nano **6**, 7034 (2012)
124. A.E. Saunders, I. Popov, U. Banin, J. Phys. Chem. B **110**, 25421 (2006)
125. J. Tiggesbäumker, L. Köller, K.-H. Meiwes-Broer, Chem. Phys. Lett. **260**, 428 (1996)